

# AI-derived 3D cloud tomography from geostationary 2D satellite data

Sarah Brüning<sup>1</sup>, Stefan Niebler<sup>2</sup>, and Holger Tost<sup>1</sup>

<sup>1</sup>Institute for Physics of the Atmosphere, Johannes Gutenberg University Mainz, Johann-Joachim-Becher-Weg 21, Mainz, 55128, Rhineland-Palatine, Germany

<sup>2</sup>Institute of Computer Science, Johannes Gutenberg University Mainz, Staudingerweg 9, Mainz, 55128, Rhineland-Palatine, Germany

**Correspondence:** Sarah Brüning (sbruenin@uni-mainz.de)

**Abstract.** Satellite instruments provide ~~spatially extended data with a high temporal resolution on almost global scales. However, nowadays, it is still a challenge to extract fully three-dimensional data from the current generation of satellite instruments, which either provide horizontal patterns~~ high-temporal-resolution data on a global scale, but extracting 3D information from current instruments remains a challenge. Most observational data is 2D, offering either cloud top information or vertical profiles ~~along the orbit track. Following this, we train~~. We trained a neural network ~~in this study to generate three-dimensional cloud structures (Res-UNet) to merge high-resolution satellite images from MSG SEVIRI satellite data in high spatio-temporal resolution. We evaluate the derived artificial intelligence-based predictions against the along-track radar reflectivity from the CloudSat satellite. By inferring the pixel-wise cloud column to the satellite's full disk, our results emphasize that spatio-temporal dynamics can be delineated for the whole domain. Robust reflectivities are derived for different cloud types with a clear distinction regarding the cloud's~~ with 2D CloudSat radar reflectivities to generate 3D cloud structures. The Res-UNet extrapolates the 2D reflectivities across the full disk of MSG SEVIRI, enabling a reconstruction of the cloud intensity, height, and shape. ~~Cloud-free pixels tend to be over-represented because of the high~~ in 3D. The imbalance between cloudy and clear-sky ~~samples. The average error (RMSE) spans about 7.5 % (3.41 dBZ) of the total value range enabling the advanced analysis of vertical cloud properties. Although we receive high accordance between radar data and our predictions, the quality of the results varies with the complexity of the cloud structure. The representation of CloudSat profiles results in an overestimation of cloud-free pixels. Our RMSE accounts for 2.99 dBZ. This corresponds to 6.6 % error on a reflectivity scale between -25 and 20 dBZ. While the model aligns well with CloudSat data, it simplifies~~ multi-level and mesoscale clouds ~~is often simplified. Despite current~~, in particular. Despite these limitations, the ~~obtained results can help close current results can bridge~~ data gaps and ~~exhibit the potential to be applied to various climate science questions, like the further investigation support research in climate science such as the analysis~~ of deep convection ~~through over~~ time and space.

## 1 Introduction

Clouds and their interdependent feedback mechanisms have been a source of uncertainty in Earth system models for decades. ~~As they influence different spheres of the environment, their accurate representation is needed for an improved understanding~~

of interconnected dynamics (Norris et al., 2016; Stevens and Bony, 2013; Vial et al., 2013). Although their connection Their  
25 influence to atmospheric gases and general circulation patterns is evident, ~~further quantification is required~~ (Rasp et al., 2018;  
Shepherd, 2014; Bony et al., 2015). ~~The pressing need to adapt society to climate change emphasizes the need for reliable~~  
~~data~~ In a world affected by climate change, we require an accurate representation of cloud dynamics today more than ever  
(~~Dubovik et al., 2021~~)(Norris et al., 2016; Stevens and Bony, 2013; Vial et al., 2013).

In recent years, observational data from remote sensing instruments ~~have been proven reliable in investigating~~ has been  
30 used to investigate cloud properties on multiple scales (Jeppesen et al., 2019). ~~Although these approaches drove research~~  
~~forward~~ Nevertheless, techniques to detect three-dimensional (3D) cloud structures ~~still need to be developed~~ (~~Bocquet et al., 2015~~)  
~~While passive sensors like geostationary satellites on a large-scale are not yet established~~ (Bocquet et al., 2015). Observations  
from passive sensors on geostationary satellites have a high spatio-temporal coverage, but they are limited to monitor the upper-  
most atmospheric layer ~~from space with a two-dimensional in two-dimensions~~ (2D) output (Noh et al., 2022)(Noh et al., 2022).  
35 By using the satellite's specificity at different wavelengths (Thies and Bendix, 2011), and subjective labeling or fixed thresholds  
(Platnick et al., 2017), we can estimate cloud physical properties like the cloud optical thickness (Henken et al., 2011) or the  
effective radius (Chen et al., 2020). In contrast, active radar penetrates the cloud top and delivers ~~detailed~~ information on the  
subjacent reflectivity distribution (Barker et al., 2011). The ~~latter provides a thorough but spatially and temporally limited~~  
~~perspective~~ (Wang et al., 2023). ~~An approximation of cloud physical properties like the cloud optical thickness, the effective~~  
40 ~~radius, or the cloud water path is obtainable using the satellite's specificity at different wavelengths~~ (Thies and Bendix, 2011; Platnick et al.,  
~~While this analysis often rests upon subjective labeling or fixed thresholds, it is under the risk of bias~~ (Stubenrauch et al., 2013)  
~~Besides, passive sensors lack the inherent sensitivity to detect information from deep within cloud layers to accurately~~  
~~differentiate cloud types~~ (Noh et al., 2022). At this point, combining radar receives detailed information on the cloud column  
along a 2D cross section with a high ground resolution and constant sun illumination. Due to its sun-synchronous orbit,  
45 it observes the same spot at the same local time. Compared to geostationary satellites, the active radar does not provide a  
continuous spatial and temporal coverage (Wang et al., 2023). Passive sensors can be used to deliver an approximation of  
the cloud vertical column, but their information density is reduced compared to active sensors (Noh et al., 2022). Combining  
data sources can ~~substantially leverage the quality of analysis~~ (Amato et al., 2020; Steiner et al., 1995). A joined fill current  
data gaps (Amato et al., 2020; Steiner et al., 1995). The combined use of different instruments ~~to derive comprehensive 3D~~  
50 ~~structures~~ has been investigated before ~~either by~~. This research comprises the usage of statistical algorithms (Miller et al.,  
2014; Seiz and Davies, 2006; Noh et al., 2022), the integration of radiative transfer approaches (Forster et al., 2021; Zhang  
et al., 2012), or the derivation of the multi-angle geometry of neighboring clouds (Barker et al., 2011; Ham et al., 2015) :  
~~The large-scale generability of these methods is expandable since their 3D results are limited to the cloud's spatial vicinity~~  
(Leinonen et al., 2019). To this day, no interpolation of to reconstruct the cloud vertical column to a large-scale, supra-regional  
55 perspective exists (Wang et al., 2023; Dubovik et al., 2021).

Emerging facilitators of data availability, like open-data policies and improved technological standards, ~~open up unforeseen~~  
~~possibilities~~ (Jeppesen et al., 2019; Liu et al., 2016; Reichstein et al., 2019). ~~These developments promote~~ enable effective processing  
of memory-consuming data (Irrgang et al., 2021; Rasp et al., 2018). This development promotes a further integration of com-

puter science methods in climate science ~~as they enable effective processing of memory-consuming satellite data (Irrgang et al., 2021; Rasp~~  
60 ~~. With an accompanying potential for substantial growth in knowledge (Amato et al., 2020; Watson-Parris, 2021), ever-growing~~  
(Jeppesen et al., 2019; Liu et al., 2016). Ever-growing quantities of data surpass the capability of the human mind to extract ex-  
plainable information efficiently (Lee et al., 2021; Karpatne et al., 2019). Here, the usage of artificial intelligence (AI) has been  
assigned a primary role (Runge et al., 2019). Cloud properties have been analyzed before ~~using by~~ Machine Learning (ML) al-  
gorithms (Reichstein et al., 2019; Marais et al., 2020), ~~but~~. The recent technological advances enable unprecedented operations  
65 ~~, especially on big data (Amato et al., 2020). Suitable (Amato et al., 2020). Deep-Learning (DL) based networks are suitable~~  
to identify spatial, spectral, and temporal patterns ~~, Deep-Learning (DL) based networks outperform classical ML approaches~~  
~~in terms of time efficiency and feasibility (Jeppesen et al., 2019; Hilburn et al., 2020; Le Goff et al., 2017). Their adaptation~~  
on big data (Jeppesen et al., 2019; Hilburn et al., 2020). In contrast to traditional ML frameworks, they do not require manual  
feature engineering (Le Goff et al., 2017). Adapting DL frameworks to applications in climate science offer new perspectives  
70 for ~~the scientific community and the general public (Rasp et al., 2018; Rolnick et al., 2022; Jones, 2017)~~ a gain in knowledge  
(Rolnick et al., 2022; Jones, 2017).

So far, ~~the possibility of investigating cloud properties by the usage of DL algorithms has been shown~~ cloud properties  
have been investigated by DL algorithms in various applications. These comprise ~~detecting and segmenting cloud fields~~  
~~(Dröner et al., 2018; Jeppesen et al., 2019; Lee et al., 2021; Le Goff et al., 2017; Tarrío et al., 2020; Cintineo et al., 2020) or classifying~~  
75 the detection (Dröner et al., 2018) and segmentation of cloud fields (Jeppesen et al., 2019; Lee et al., 2021; Le Goff et al., 2017; Tarrío et  
, or the classification of distinct cloud types from meteorological satellites and aerial imagery (Marais et al., 2020; Wang et al.,  
2023). Zantedeschi et al. (2022) used a neural network to bring together information from an active radar and high resolved  
satellite image data to reconstruct cloud labels. Regressive models were used to ~~investigate the delineation of~~ predict rain  
rates (Han et al., 2022) or convective onset (Pan et al., 2021) for an improved weather forecast. ~~While the results indicate~~  
80 ~~an improvement in resource efficiency, they are predominately restricted to horizontal processes of~~ These studies are often  
limited to reflect horizontal processes within the cloud field. ~~Reconstructing the cloud vertical column can deliver insights~~  
~~into 3D dynamics (van den Heuvel et al., 2020; Leinonen et al., 2019).~~ Current studies by Hilburn et al. (2020) and Leinonen  
et al. (2019) use AI techniques such as convolutional neural networks (CNN) and conditional generative adversarial net-  
works (CGAN) to address this issue. ~~In both cases, they provide pixel-based cloud reflectivities similar to the input of an~~  
85 ~~active radar (Wang et al., 2023). Nevertheless, the~~ They reconstruct the 1D cloud column (Hilburn et al., 2020) or the 2D  
cross section of the input data (Wang et al., 2023). To our best knowledge, no extrapolation of 2D radar data to a large-  
scale spatial coherence cannot be fully resolved. Prior studies face limitations when predicting 3D perspective was conducted  
before (Wang et al., 2023; Dubovik et al., 2021). Clouds move within a 3D space. This limits the prediction of multi-layer  
and mesoscale events ~~(Hilburn et al., 2020). Since clouds in the real world are highly complex, spatially restricted models~~  
90 by a 1D or 2D pixel-wise reconstruction (Hilburn et al., 2020). Models that do not consider the spatial coherence between  
pixels fail to reconstruct comprehensive cloud structures (Hu et al., 2021). Image ~~prediction segmentation~~ approaches like  
the UNet (Ronneberger et al., 2015; Jiao et al., 2020; Wieland et al., 2019) ~~display a promising start to~~ may reconstruct  
the ground truth data ~~and more adequately. They can be used~~ to provide the indicators for predicting clouds in 3D with

its adjacent boundaries, shadow locations, and geometries ~~-. Defining each cloud as a connected entity (Wang et al., 2023).~~

95 ~~This~~ can lead to a more realistic representation of the ~~actual distribution of clouds and their interactions around the globe~~  
~~(Jiao et al., 2020; Hu et al., 2021; Wang et al., 2023)~~ predicted clouds (Jiao et al., 2020).

~~This study combines the benefits of active and passive instruments by~~ In this study, we employ a modified Res-UNet (Di-  
akogiannis et al., 2020; Hu et al., 2021) to ~~reconstruct the~~ integrate 2D data from active (polar orbiting satellite, radar) and  
100 passive (geostationary satellite, spectrometer) instruments to reconstruct a 3D ~~vertical cloud column of volumetric radar data~~  
~~from 2D geostationary satellite data. In contrast to former studies focusing on the pixel-based perspective along the radar track,~~  
~~the spatial connectivity between individual pixels is preserved~~ cloud field. Previous studies focused on reconstructing the 1D  
cloud column or 2D cross section. In contrast, our approach utilizes a DL framework to predict the ~~results for the spatial extent~~  
~~of the input image and infer them to a large-scale area on the~~ radar reflectivity not only along the radar cross section but  
across the entire satellite full disk (FD). We use the radar height levels to extend 2D satellite channels into a 3D perspective.  
105 The goal is to ~~derive~~ establish a spatio-temporal consistent cloud tomography ~~based exclusively on real-world data. This~~  
~~information can be used to improve the availability and quality~~ solely based on observational data. Predicted reflectivities can  
enhance the availability of 3D resolved cloud structures, ~~especially in data-sparse regions~~, and their further investigation in a  
hydro-climatological context particularly in regions with limited data.

## 2 Methods

### 110 2.1 Data overview

Our approach uses observational data from two different remote sensing sensors to predict a 3D cloud tomography. The  
input data for the ~~network originates~~ neural network originates from a geostationary satellite. We use data from the European  
Organisation for the Exploitation of Meteorological Satellites (EUMETSAT) Spinning Enhanced Visible and InfraRed Imager  
(SEVIRI) instrument on the Meteosat Second Generation (MSG) satellite (EUMETSAT Data Services, 2023). This sensor  
115 observes the Earth ~~surface from space providing~~ from a height of 36000 km and provides 2D image data in a high spatial  
and temporal resolution. The ground truth of the study is derived from an active radar ~~orbiting the globe on a sinusoidal track~~  
~~(CloudSat Data Processing Center, 2023). It receives on board the CloudSat satellite which moves on a sun-synchronous orbit~~  
~~(CloudSat Data Processing Center, 2023). The 2D profiles along the track contain~~ information on the cloud reflectivity during  
this flight, point by point, which are combined into vertical profiles. Here, In our study, we feed the ~~satellite data into the~~  
120 ~~model to delineate the relationships needed to accurately reconstruct these profiles~~ MSG SEVIRI data into a neural network to  
reconstruct the CloudSat radar reflectivity and extrapolate the 2D profiles to a 3D perspective.

#### 2.1.1 Satellite Geostationary satellite data

~~Data from the European Organisation for the Exploitation of Meteorological Satellites (EUMETSAT) Spinning Enhanced~~  
~~Visible and InfraRed Imager (SEVIRI) instrument on the Meteosat Second Generation (MSG) satellite~~ Image data from

**Table 1.** Overview of MSG SEVIRI channels (Schmetz et al., 2002).

Channel	Center ( $\mu\text{m}$ )	Range ( $\mu\text{m}$ )	Solar (reflectance)
VIS0.6	0.635	0.56-0.71	yes
VIS0.8	0.81	0.74-0.88	yes
NIR1.6	1.6	1.5-1.78	yes
IR3.9	3.92	3.48-4.36	daytime
WV6.2	6.25	5.35-7.15	no
WV7.3	7.35	6.85-7.85	no
IR8.7	8.70	8.30-9.10	no
IR9.7	9.66	9.38-9.94	no
IR10.8	10.8	9.80-11.80	no
IR12.0	12.0	11.00-13.00	no
IR 13.4	13.4	12.40-14.40	no
HRV	n/a	0.5-0.9	yes

125 the MSG SEVIRI instrument displays the input for the network (later referred to as "satellite data") (Schmetz et al., 2002).  
Observing the Earth's surface in intervals of 15 min and with a spatial resolution of 3 km at nadir, ~~it~~ MSG SEVIRI pro-  
vides information in 11-12 channels centered within wavelengths from 0.6–132  $\mu\text{m}$  (Benas et al., 2017). ~~While the first three~~  
Depending on the wavelength and daytime of retrieval, the channels are sensitive to reflected solar radiation ~~, the others measure~~  
~~surface emissions within the near to thermal infrared spectrum. These channels~~ or surface emissions (Table 1). They can be  
130 applied to approximate cloud physical properties (Sieglaff et al., 2013). ~~Regions close to the poles are discarded due to reduced~~  
~~sensor accuracy at the satellite's outer~~ Our approach uses 11 channels. The HRV channel is excluded due to its different  
resolution and uncertain added value. Three of the channels are sensitive to solar radiation, which restricts us to using only  
135 daytime data. We reformat all satellite images onto a spatial grid with geographic coordinates, employing the global reference  
system WGS84 (Dröner et al., 2018). Each pixel has a resolution of 0.03 ° in both width (W) and height (H). To account for  
diminishing accuracy from the equator to the poles, we exclude the areas near the sensor boundaries (Bedka et al., 2010). The  
final designated area of interest (AOI) ~~comprises an extent between~~ extends 60 ° in all directions ~~and represents~~ , marking the  
boundaries of the new FD. ~~All satellite images are resampled to a geographic grid using the global reference system WGS84~~  
~~(Dröner et al., 2018).~~

### 2.1.2 Radar data

140 Within the CloudSat (CS) GEOPROF-2B product, a nadir-looking 94 GHz ~~active radar~~ cloud profiling radar (CPR) delivers  
information on the cloud reflectivity in logarithmic dBZ scale (later referred to as "radar data") (Stephens et al., 2008). The  
radar ~~scenes reflect the predominant cloud structure at the given transect~~ receives a 2D cross section of the cloud column with a

horizontal resolution of 1.1 km and a vertical. The vertical dimension (Z) comprises 125 height levels with a bin size of 240 m in 125 height levels (Guillaume et al., 2018). The total vertical extent comprises 0–30 km, from the mean (Guillaume et al., 2018) . From the ground surface to the lower stratosphere. Information on the reflectivity obtained by the radar displays, the vertical extent covers 30 km. We use the reflectivity transects as the ground truth used to train and evaluate the model results. In the subsequent steps, we adjust the height levels of the radar. The lower altitudes, specifically those between 0 and 3 km, are influenced by the topography and a radar signal weakening due to attenuation (Marchand et al., 2008). To enhance the model performance, we omit the lowest 10 height levels. Since we notice a significant imbalance between clear-sky and cloudy pixels, we exclude the predominantly cloud-free areas within the upper 25 height levels (Stephens et al., 2008). The final Z-dimension encompasses 90 height levels ranging from 2.4 km to 24 km. We note that due to the sun-synchronous orbit of CloudSat, it has a reduced ability to account for diurnal variations within specific regions of the AOI (Stephens et al., 2008).

### 2.1.3 Matching scheme

Matching the MSG SEVIRI scenes and the overflight of the CloudSat radar extracts the training data of the study. The framework automatically identifies the radar overpass over the satellite domain and its flight direction (Fig. 1). Figure 1 pictures a schematic view of the matching scheme. First, the We obtain training data for our study by aligning MSG SEVIRI scenes with CloudSat radar data as shown in Figure 1 (a). To match the datasets, we compare their timestamps and locations of both data sources are compared. Suppose the current flight coordinates lie within the satellite AOI. In that case, the direction of flight is determined by the coordinates of the first and last entry of the radar file. The most northward and southward locations define the radar's direction as. If the radar coordinates fall within the AOI of the satellite, we determine the flight direction to identify whether CloudSat circles the Earth in ascending or descending. We place the first image at the lower-right or upper-left corner of the radar within the satellite FD. To derive continuous tracks, orbit. We then extract images of 128 x 128 [H x W] pixels from each MSG SEVIRI channel along the radar coordinates using a moving-window approach is applied with a 50 % overlap between single images starting with the most northern (descending) or southern (ascending) location (Denby, 2020; Jeppesen et al., 2019). Each image contains the native satellite channels leading to an input size of image-profile pairs (Denby, 2020; Jeppesen et al., 2019).

We prepare the matched image-profile pairs for further processing. To do this, we combine the 11 MSG SEVIRI channels into a single 3D array with dimensions 11 x 128 x 128 pixels [C x X x Y. The radar track is centered within each image displaying the vertical column along the horizontal transect Z x XY [H x W] (Fig. 1). A spatial join of the radar data coordinates fits the resolution between both sensors. For that purpose, pixels. CloudSat flies across a horizontal transect within the satellite scene. It has a higher native resolution than MSG SEVIRI. To align the datasets, we downsample the radar pixels by aggregating them based on the local maximum reflectivity of each pixel area returns the factor to coarse-grain the radar data. This filter results in a partial information loss at the edges of individual clouds (Jordahl et al., 2020). This adjusts the CloudSat pixels to the MSG SEVIRI resolution of 0.03 ° but leads to some loss of sharp contrast in radar pixels (Jordahl et al., 2020). We standardize the data shape by transforming the 2D cross section into a sparse 3D array of 125 x 128 x 128 [Z x H x W] pixels, representing reflectivities along the cross section. After downsampling, the transect becomes one-pixel wide. We label pixels outside the

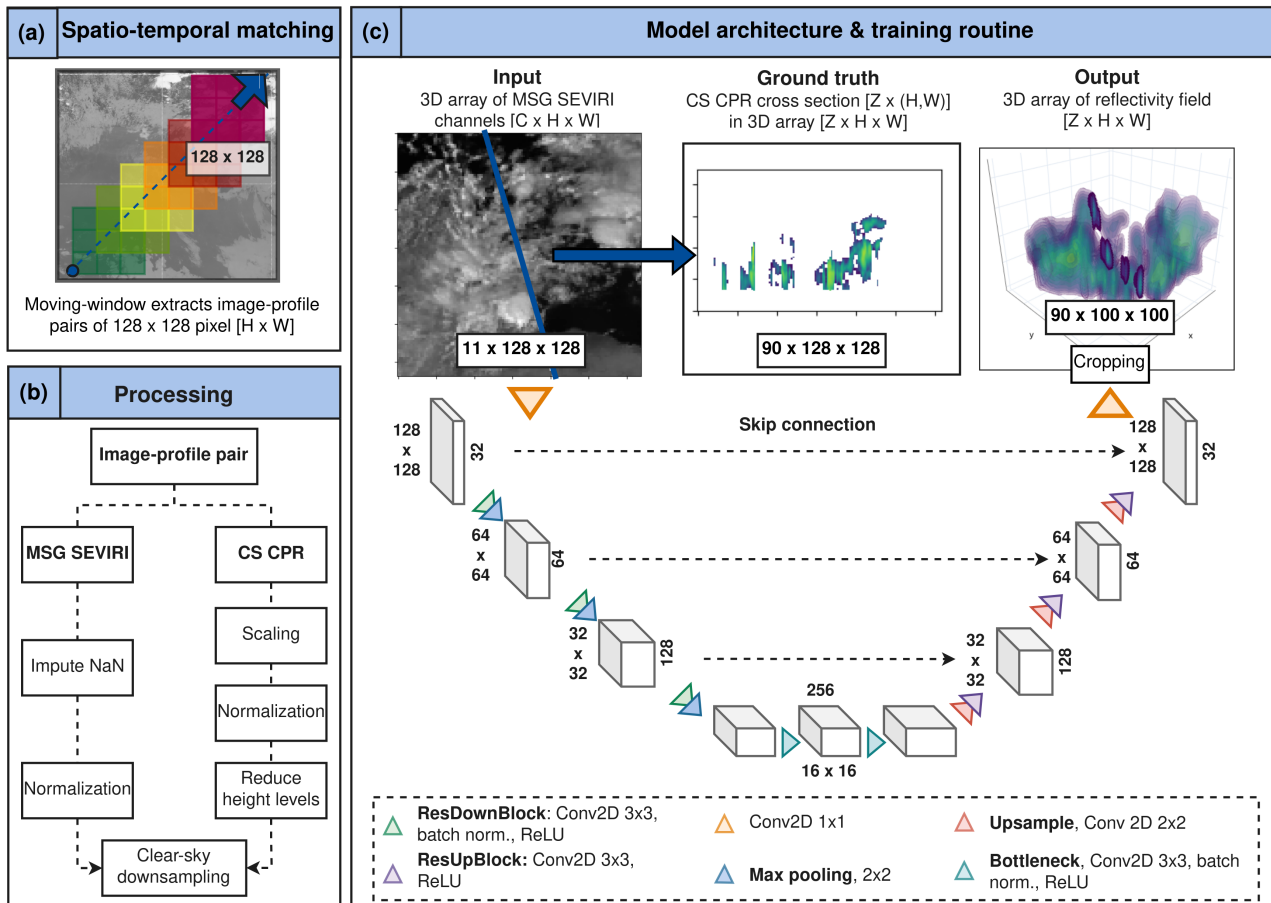


**Figure 1.** Workflow of the study. Part (1)(a) points out the moving-window approach used for matching the radar and the satellite data. Steps needed for the processing of both datasets is are depicted in (2)(b). In (3)(c), the architecture of the proposed Res-UNet is pictured-alongside illustrated. The upper row visualizes an example for the input data, ground truth (with reduced 90 height levels and full transparency for values  $\leq -25$  dBZ), and predicted-output respectively. In the-output-sample, the-The location of the radar transect within the 3D output image is pictured with full opacity. Each-numbered-box refers The numbers alongside the boxes in the architecture sketch refer to the feature channels (right) and image sizes (left) at the given model depth.

transect as missing values to maintain the CloudSat data's location during training. We use these pixel indices to compute the loss between the CloudSat data and the predicted cross section and to evaluate the model performance.

## 2.1.4 ~~Processing~~Data processing

180 ~~Extracted satellite samples display the physical predictors fed into the network to reconstruct the vertical cloud distribution. Using a whole~~ Before training the model, we process the extracted image-profile pairs. We utilize a full year of data (2017) ~~integrates to incorporate~~ seasonal variations into the modeling routine, leading to 30,000 samples. From these, ~~process.~~ We split ~~the 30000 matched image-profile pairs, with 75 % went into training the model (January to September) used for training and 25 % into its evaluation.~~ Since the radar data distribution is highly skewed towards clear-sky samples, reducing the percentage ~~of cloud-free ground truth in the final dataset to 10 % tackles this imbalance (Jeppesen et al., 2019). This threshold accounts for the classification of whole samples, not the proportion within single images. Nevertheless, a cloudy scene can still consist of a big proportion of background pixels (Fig. 1).~~ Data ~~(October to December) for validation. Our test set is derived from data in May 2016, from which the matching algorithm extracts 1500 image-profile pairs. We impute missing data in the 3D MSG SEVIRI array by an interpolation of neighbouring pixels (Troyanskaya et al., 2001). Afterwards, data~~ from each satellite   
185 channel  $x$  was normalized between ~~[-10,1]~~  $[-1,1]$  by

$$x' = \frac{x - \mu}{\sigma} \quad (1)$$

using the arithmetic mean  $\mu$  and standard deviation  $\sigma$  of the training data (Leinonen et al., 2019). ~~The technical limitations of the sensor require rescaling all radar tracks between 20 dBZ and -25 dBZ. Reducing the data to 90 height levels between 2.4 and 24 km minimizes the influence of the topography and higher atmosphere. Otherwise, the high attenuation degrades~~   
195 ~~the quality flag of the CloudSat radar in high and low altitudes. Smoothing the CloudSat values by its internal quality flag diminishes noise within the samples (Marchand et al., 2008). Here, pixels~~ As described in Section 2.1.2, we reduce the height levels of the CloudSat profile from 125 to 90 (Fig. 1, b). We use the CloudSat quality index to identify noisy pixels. Pixels with ~~a quality index~~ lower than six were ~~classified as missing values and~~ set to a background value of -25 dBZ. ~~After the quality assessment, all~~ to reduce noise (Marchand et al., 2008). All radar reflectivity values  $Z_{dB}$  were normalized ~~to~~ ~~between~~  $[-1,1]$  as   
200 follows

$$Z'_{dB} = 2 \frac{Z_{dB} + 35dB}{55dB} \pm 1 \quad (2)$$

by the maximum and minimum ~~reflectivity between~~  $[-35, 20]$  ~~of the value range (Stephens et al., 2008; Leinonen et al., 2019)~~ ~~(Stephens et al., 2008; Leinonen et al., 2019). The CloudSat data is highly skewed towards clear-sky samples. We limit the percentage of cloud-free profiles to 10 % to tackle this imbalance (Jeppesen et al., 2019).~~

## 205 2.2 Model architecture and training

~~The backbone of the study rests upon the Res-UNet architecture (LeCun et al., 2015; Ronneberger et al., 2015). While the UNet is well established for tasks from vision computing, evaluating its feasibility for environmental data is still in progress~~



(Dixit et al., 2021) Neural networks can capture highly complex relationships between input and output data (Lee et al., 2021). The Res-UNet used in this study displays a modified framework designed for the use-case of remote sensing data. By adding (Dixit et al., 2021). Additional residual connections and continuous pooling operations, aim to reduce the dependence of the network on the input's location is reduced (Diakogiannis et al., 2020). Former studies dealing using the Res-UNet dealt with the classification of tree species (Cao and Zhang, 2020), the segmentation of buildings (Dixit et al., 2021), or the delineation of precipitation intensity (Zhang et al., 2023) emphasize or the potential prediction of precipitation (Zhang et al., 2023). Obtained results emphasize the ability of the Res-UNet to adequately address the importance of the spatial coherence in a dynamic environment environmental research (Marais et al., 2020). In this study, the regression derives we derive the cloud reflectivities in dBZ for each pixel in a three-dimensional image field (Hilburn et al., 2020; Leinonen et al., 2019; Zhang et al., 2023). By seeking non-linear approximations of between the input and the output data, the neural network can detect complex relationships between the variables (Lee et al., 2021) from the satellite channels by a regression task (Hilburn et al., 2020; Zhang et al., 2023).

As introduced by Ronneberger et al. (2015), the UNet and its modifications provide an almost symmetrical architecture. Figure 1 illustrates the network architecture whereas each convolution is expanded by the structure of a residual block as described by Diakogiannis et al. (2020). Following a sequence of down-sampling layers on the encoder side, the original spatial extent of 128 x 128 pixels is reconstructed by continuous up-sampling layers in The network architecture of the decoder side (Lee et al., 2021). To maintain the spatial coherence in the last down-sampling layer, the model depth is restricted to 4 subsequent convolutions. Each residual block consists of a convolution with a kernel size of Res-UNet is shown in Figure 1 (c). The parameters of the network are listed in Table A1 in Appendix A. Each box represents the layer sizes on the encoder and decoder side. On the right side of each box, the filter size is given. The respective height and width are given on the left side.

The Res-UNet consists of six residual blocks, each including two 2D convolutions (3 x 3 and shortcut connections used to avoid model degradation (Diakogiannis et al., 2020). A batch normalization layer and an activation layer with a rectified linear unit (ReLU) follow the convolution of the input layer for improved robustness and to avoid extreme values (Le Goff et al., 2017; Li et al., 2020). A maximum pooling of size 2 kernel, stride 1) and ReLU activation (Diakogiannis et al., 2020). On the encoder side, we add batch normalization. The output is merged with a skip connection that consists of one 2D convolution (3 x 3 kernel, stride 1), and a batch normalization. Adding the skip connection and the convolutional layer represents the output of a residual block.

We increase the channel dimension of the initial satellite image from 11 x 2 reduces the initial spatial extent from 128 x 128 pixels with a 1 x 1 2D convolution to a feature map of size 32 x 128 x 128. In the encoder branch, we then employ a sequence of three residual blocks with doubling filter sizes, each followed by a 2 x 2 max pooling layer (Lee et al., 2021). We subsequently reduce the feature map size to 64 x 64 pixels (Lee et al., 2021). Repeating this routine of operations for every layer in the encoder, we halve the image size every time while doubling the number of feature channels leading to a final size of 256 x 8 x 8 pixels (Ronneberger et al., 2015). After the last pooling layer 16 x 16 pixels in the bottleneck layer. Here, we apply a sequence of repeated convolutions two 2D convolution layers followed by batch normalization and a ReLU activation.

On the decoder side, a likewise sequence of upsampling blocks accompanied by features originating skip connections expands the low-resolution image to its original extent but with a modified representation (Li et al., 2018). In this case, these are the 3D radar reflectivities. The upsampling displays the inversion of the pooling on the encoder side, doubling the spatial extent to fit the size of the ~~The decoder side features three residual blocks, each with an upsampling layer (2D convolution, 2 x 2 kernel, stride 2) and a corresponding skip connection. In each step, the upsampling is followed by from the encoder. After upsampling, we apply a residual block with a convolution and a ReLU activation layer ((Lee et al., 2021)). After the last upsampling block, a convolution with a kernel size of 2D convolution (3 x 3 kernel, stride 1) and ReLU activation, doubling the spatial extent to match the skip connection while halving the channel dimension (Li et al., 2018). The final 1 x 1 convolution~~ maps the output to ~~a size of 90 x 128 x 128 pixels. A subsequent removal of the outermost pixels leads to a final size, representing the 90 height levels of the radar cross-section (Jeppesen et al., 2019). We remove the border pixels of the output, resulting in a final radar reflectivity output of 90 x 100 x 100 pixels (Jeppesen et al., 2019)[C x W x H]. Predicted reflectivities are scaled between -35 and 20 dBZ, with values below -25 dBZ considered as cloud-free (Leinonen et al., 2019).~~

~~Choosing~~ We conducted the training for 50 epochs with a batch size of 4 and a weight decay of 0.00001 (see Table A1 in Appendix A). We have 1893328 total trainable parameters. The estimated total size of the model is 194.27 MB (see Table B1 in Appendix B). We use the Adaptive Moment Estimation (ADAM) method ~~ensures for~~ model optimization due to its fast convergence rate (Kingma and Ba, 2014). ~~As flipped images are perceived as new samples, we~~ The learning rate is initially set to 0.001 (see Table A1 in Appendix A). It is reduced by a learning rate scheduler during the training process when reaching a plateau. To enhance the amount of training data ~~by giving all samples,~~ we give all input data a chance of 25 % to be ~~either vertically or horizontally rotated (Jeppesen et al., 2019). Predicted reflectivities are matched to the CloudSat value range with a lower limit of -25 dBZ to differentiate a cloud signal from background noise (Leinonen et al., 2019) rotated by 90 ° (Jeppesen et al., 2019). These flipped images are perceived as new samples. The goal is to increase the model invariance to the orientation of the radar cross section.~~

## 2.3 Evaluation

### 2.3.1 Model Analyzing and comparing the model performance

The model performance is ~~evaluated by~~ quantified during training (loss function) and evaluated afterwards by calculating the root-mean-square error (RMSE) ~~, which equally penalizes~~ (see Table A1 in Appendix A). The RMSE is equally able to penalize misses and false alarms (Lee et al., 2021). ~~Since ground truth is limited to the radar overpass, only~~ As described in Section 2.1.3, we preserve the pixel indices of the CloudSat cross section within each image-profile pair during training. We use the location of these pixels to filter the observed and predicted transect. The RMSE is calculated along the filtered cross sections. ~~Since it is only evaluated on a small subset of 10 % of the pixels are used for the error calculation (Wang et al., 2020). The loss is calculated according to:-~~

$$RMSE = \sqrt{\sum_{i=1}^D (x_i - y_i)^2}.$$

275 The results of the DL network are compared against two pixel-based methods to examine its performance along the radar track. Training data for these approaches is extracted from the previously created dataset. For each image, the horizontal diagonal of the radar overpass is divided into pixel-wise training samples along the XY-axis. The final input consists of an array of 11 satellite channels. Each ground truth sample displays an array of 90 height bins along the Z-axis (Fig. 1). Preserving the index of the pixel along the diagonal during the training routine allows a reconstruction of the radar track. Both models utilize the normalized satellite data to reconstruct the radar reflectivity (Sect. 2.1.4). The RMSE is calculated after rescaling  
 280 ~~the output back to the dBZ scale~~ of all pixels, we have a sparse regression task (Wang et al., 2020). We cannot quantify the model performance on the full 3D prediction of the cloud field.

The results of the Res-UNet are compared against two competitive methods (Dröner et al., 2018). First, ~~this study applies we predict the radar reflectivity by~~ an ordinary least squares model with multiple regression output (OLS) ~~as a baseline model (Miller et al., 2014). In this case, all~~. The 11 satellite channels were used as independent predictor variables ~~to estimate~~  
 285 ~~the radar reflectivity for each pixel along the~~. The output is a 1D cloud column. Second, a Random-Forest (RF) regression is applied (Wang et al., 2021). ~~As (Breiman, 2001). The RF is~~ a supervised ML algorithm, ~~the RF pictures a robust method suitable~~ when working with large environmental datasets in the natural sciences (Boulesteix et al., 2012). ~~In the past, numerous studies investigated its~~ Its feasibility for complex meteorological data ~~was investigated before~~, e.g., ~~detecting clouds (McCandless and Jiménez, 2020) or delineating rain rates (Kühnlein et al., 2014). This study tested a minimal~~ McCandless and Jiménez  
 290 ~~used a RF regression to detect clouds. Our study uses a~~ setup with 100 trees, each choosing a random subset of ~~predictors (McCandless and Jiménez, 2020). Both models~~ satellite channels to predict the reflectivity along a 1D cloud column. We use the same ~~data split as training, validation and test split as for the Res-UNet (Sect. 2.1.4). After training, the original radar track is restored to enable a track-wise comparison. For each image-profile pair, we filter the 3D array to locate the radar cross section. This transect is separated into 1D cloud columns. For every pixel along the cross section, we receive a ground truth in the shape~~  
 295 ~~of 90 x 1 [Z x (H,W)]. The 3D array containing the satellite channels was filtered by the radar profile location and divided into images of the size 11 x 1 [C, (H,W)]. The OLS and RF map the satellite image to an output size of 90 x 1 pixels [Z x (H,W)]. We calculate the RMSE between the observed and predicted cloud column and scale the output between -35-20 dBZ. We reconstruct the 2D transect by the preserved index of each pixel of the cross section. These profiles are compared to the output of the Res-UNet.~~

### 300 2.3.2 Comprehensive predictions ~~Merging 3D reflectivities on the FD~~

~~A~~ We predict the radar reflectivity for each MSG SEVIRI file in the test dataset (May 2016) using the trained Res-UNet. The result is a contiguous 3D cloud tomography ~~can be achieved by dividing the satellite FD into~~ for every 15 minute time step. The MSG SEVIRI FD covers an extent of 2400 x 2400 pixels. For the FD prediction, we divide the FD into overlapping

~~subsets of 128 x 128 pixel-subsets. These images are individually pixels. These subsets are~~ processed and fed into the network.  
305 ~~Combining their outputs of~~ The output is a 3D reflectivity image of 90 x 100 x 100 pixels ~~into a joined 3D prediction of 2400~~  
~~x 2400 pixels enables a whole satellite gridecoverage. This comprehensive cloud tomography is derived for every time step of~~  
~~the satellite dataset and is used~~ [Z x H x W], which equals 2.5 ° on the MSG SEVIRI grid. We merge the tiles to cover the  
whole satellite AOI. Between the tiles, there is no overlap. The goal is to evaluate the network's ability to ~~create a smooth~~  
~~interpolation of~~ extrapolate a large-scale cloud ~~fieldsfield from single tiles.~~

### 310 2.3.3 ~~Cloud~~ Computing the cloud top properties

~~Since neither simulations nor observational-based models deliver comparable data, the predictions are interpreted~~ To our best  
knowledge, there exist no comparable datasets to the 3D cloud tomography in this study. Instead of a quantitative evaluation  
of the reflectivity, we evaluate the predictions based on their ~~applicability for deriving cloud-top properties (Wang et al., 2023)~~  
~~At first, CloudSat data and track-wise predictions are used to compute performance to derive~~ the cloud top height (CTH)  
315 ~~for the validation data~~ (Wang et al., 2023). We use the FD predictions for the test dataset (May 2016) for the computation. The  
CTH is defined as the distance between the ground surface and the uppermost cloud layer for every 1D vertical column (Huo  
et al., 2020). This calculation requires converting the ~~CloudSat height bins height levels~~ into a kilometer scale. ~~Values with~~  
~~a reflectivity higher than~~ We use a fixed threshold of -15 dBZ display a cloudy signal, whereas lower values are classified  
~~as the background class to differentiate a cloudy from a clear-sky pixel~~ (Marchand et al., 2008). The ~~final output displays an~~  
320 ~~aggregation on a monthly scale. Afterward, the CTH result is a binary classification for each pixel in the 3D cloud field. On~~  
~~this dataset, we extract the CTH as the top cloud signal on each 1d cloud column of the FD~~ 3D reflectivities is compared. We  
aggregate the results on a monthly scale and compare the predicted CTH to the operational product CLAAS-V002E1 (CLOUD  
property dAtAset using SEVIRI, Edition 2) (Finkensieper et al., 2020). ~~Based~~ It is based on the MSG SEVIRI channels and  
additional model data ~~, CLAAS-V002E1 and~~ provides information on the macrophysical and microphysical cloud properties.  
325 ~~It is available as~~ We use a monthly aggregate with a resolution of 0.05 ° on the MSG SEVIRI FD. ~~The goal is to rate the~~  
~~predicted CTH compared to CLAAS-V002E1 by pointing out the overall agreement and regional differences.~~

### 3 Results

#### 3.1 Evaluating the model performance reflectivity distribution

330 Comparison of the height dependent RMSE for every height bin between 5–24 km and the mean error for all models calculated on the validation dataset.

Joint plot of the normalized difference between the observed and predicted reflectivity. The deviation on each height bin between 5–24 km is compared for the Res-UNet (a), the ordinary least squares model (OLS) (b), and the Random-Forest regression (RF) (c).

335 Three models were trained to compare the performance of the different approaches (Sect. 2.3.1). Due to the applied CloudSat quality flag, predictions below 5 km are influenced by the high amount of background values at -25 dBZ. We analyze the ability of the three models (Res-UNet, OLS, and RF) to reconstruct the cloud vertical distribution for the test dataset in May, 2016 (Sect. 2.1.4). As a consequence, the following evaluation refers to the predicted reflectivity above 2.3.1). The OLS and RF predict a 1D column whereas the output of the Res-UNet comprises a 3D image of the cloud field. We filter all outputs by the preserved location of the radar cross sections to derive the original 2D transect. At first, we compute the height dependent reflectivity distribution of the CloudSat data and the three models. Due to the applied quality flag (Sect. 2.1.4), we have few observations below 5 km. The results illustrate a substantial improvement when applying a DL framework compared to the OLS and RF. Figure 2 illustrates the variance of the error between 5–24 km. The mean RMSE varies between 3.41 dBZ for the Res-UNet and 4.91 dBZ (RF) or 5.27 dBZ (OLS). This difference depicts a reduction of the total error from 11.7% (OLS) or 10.9% (RF) to 7.5% for the DL network. The overall RMSE and the difference between the models reach their maximum in low altitudes km height (Fig. 2, a). This leads to a shift in low height levels. The models overestimate cloud-free values below -25 dBZ. The CloudSat reflectivities have a peak at 0–10 dBZ between 5–7 km height. In higher altitudes with more uniform clouds, the performance of all models improves. Nevertheless, the DL network outperforms the other approaches at every height level. A second, weaker peak is observed between 12–15 km for reflectivities < 0 dBZ. All predictions underestimate the first peak > 0 dBZ. Instead, they overestimate the occurrence of reflectivities < -20 dBZ (Fig. 2)-, b-d). The OLS shows an especially high shift towards low reflectivities. The Res-UNet predicts low reflectivities < -20 dBZ along all height levels between 5–15 km whereas we observe a distinct peak at 5 km for the RF.

340  
345  
350

To evaluate the accuracy of the models on different height levels, the normalized difference between the observed and predicted reflectivities is analyzed by a two-dimensional joint distribution plot. For this purpose, we calculate the density distribution of the reflectivity between 2.4–24 km. Here, we use a bin size of 1 dBZ and 240 m height, respectively (Steiner et al., 1995). All models deviate distributions are calculated on the test dataset and normalized by the distribution size ( $n = 1500$ ). Predictions differ from the original radar data, especially for values > 0 dBZ and in low altitudes (Fig. 3). The differences get smaller in higher parts of the troposphere and tropopause. A diagonal of high agreement with the observed data from high altitudes with low reflectivities to lower altitudes with higher reflectivities can be observed with the steepest diversion for the OLS. Appearing in the joint plot, the highest agreement appears in the shape of two contrasting parts, the direction differs between the Res-UNet and the other models. That said, the DL network indicates an underestimation a

355  
360

curved line between low reflectivities > 15 km to high reflectivities at 7 km. The results indicate an overestimation of high reflectivities and an ~~overestimation-underestimation~~ of low reflectivities, especially for low-level clouds. ~~Predictions in higher altitudes represent a smaller deviation from the ground truth. The other models show an overestimation of high reflectivities and an underestimation of low values in both, low- and mid-altitude. In terms of total deviation from the ground truth, Since~~  
365 ~~we observe few clouds in high altitudes (Fig. 2, a), the distribution differences get smaller above 15 km. The joint plot shows a similar distribution for the Res-UNet and the~~ Res-UNet performs best out of RF, whereas the error of the ~~three proposed models~~ Res-UNet is slightly lower for reflectivities between -15–0 dBZ (Fig. 3, a, c). We observe few predictions > 0 dBZ and a strong overestimation of reflectivities < -20 dBZ for the OLS (Fig. 3, b).

### 3.2 Analysis of cloud-vertical properties

370 Figure 4 depicts the model predictions and the observed CloudSat reflectivities along the radar track for four samples. All models detect the horizontal location of different clouds along the XY-axis. A detailed view of the individual radar tracks illustrates the transferability of the proposed DL method. In contrast to the RF and OLS, the

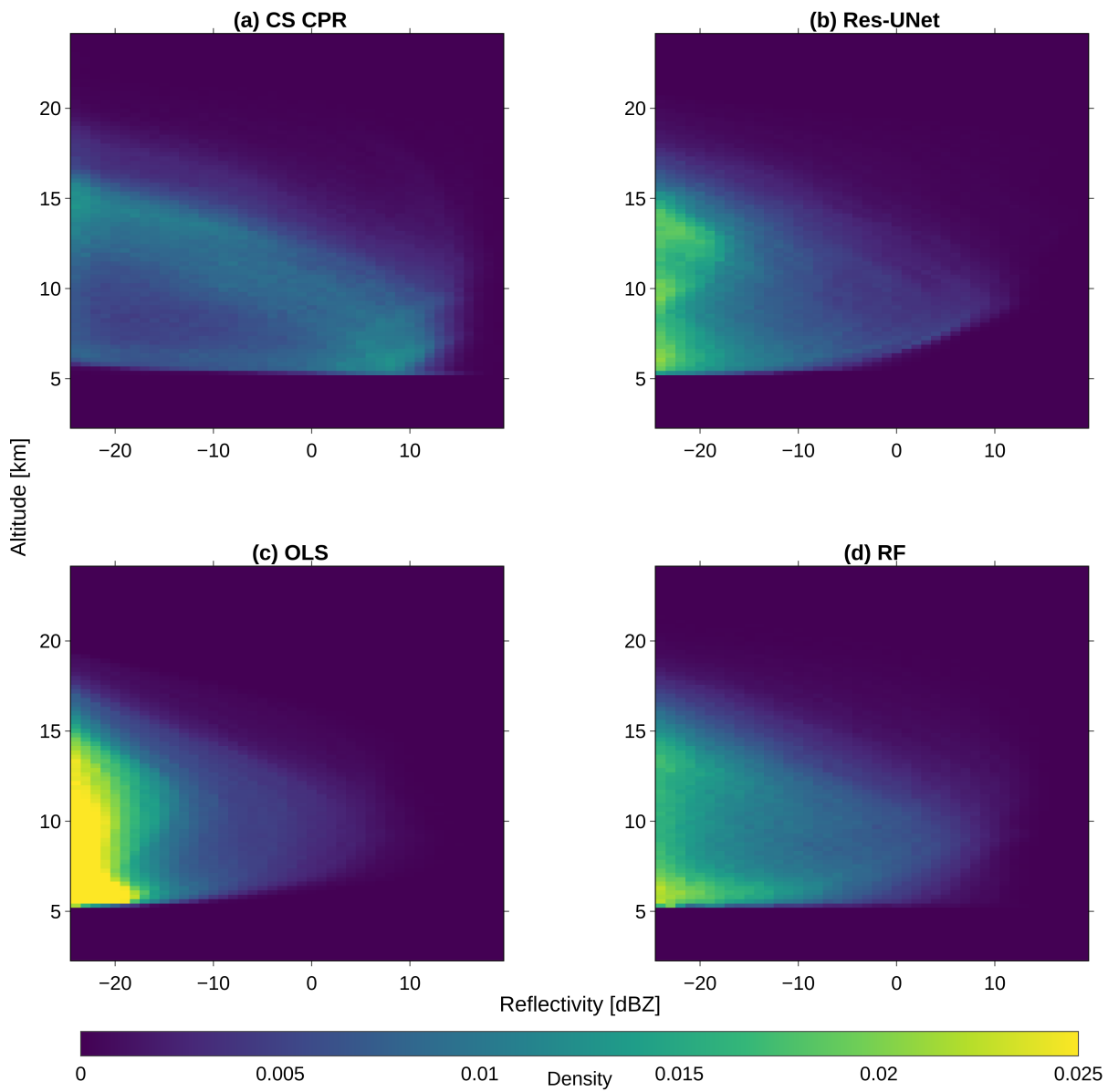


**Figure 2.** [Height dependent reflectivity distribution for every height bin between 2.4–24 km for the CloudSat data \(CS CPR\) \(a\), the Res-UNet \(b\), the ordinary least squares model \(OLS\), \(c\), and the Random-Forest regression \(RF\) \(d\) \( \$n = 1500\$ \).](#)

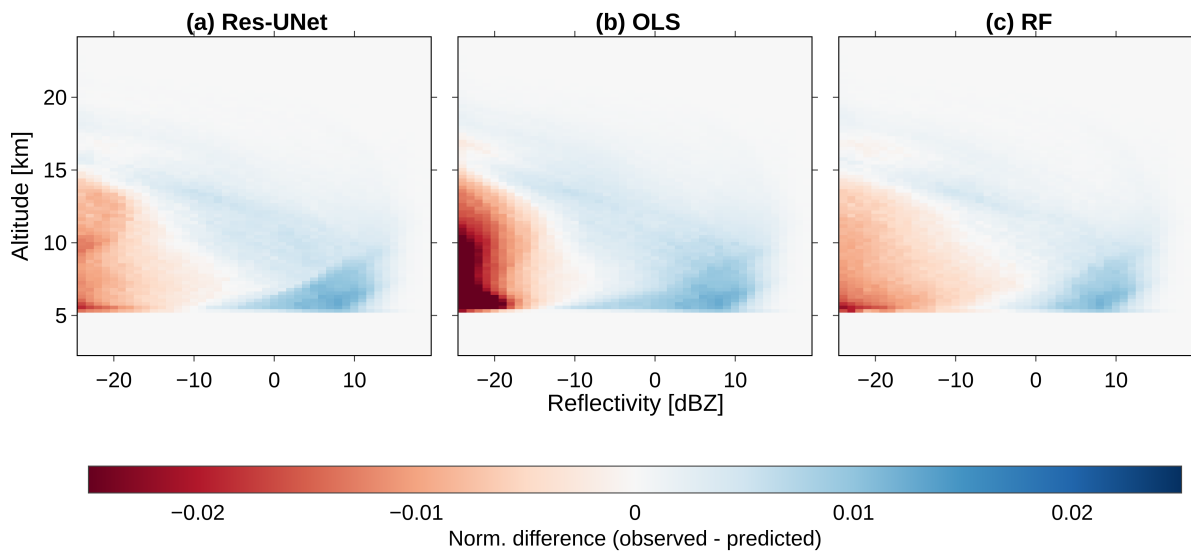


**Figure 3.** Joint plot of the normalized difference between the observed and predicted reflectivity on the test dataset ( $n = 1500$ ). For each height bin between 2.4–24 km, we compare the CloudSat density distribution (CS CPR) to the distribution of the Res-UNet (a), the ordinary least squares model (OLS) (b), and the Random-Forest regression (RF) (c).



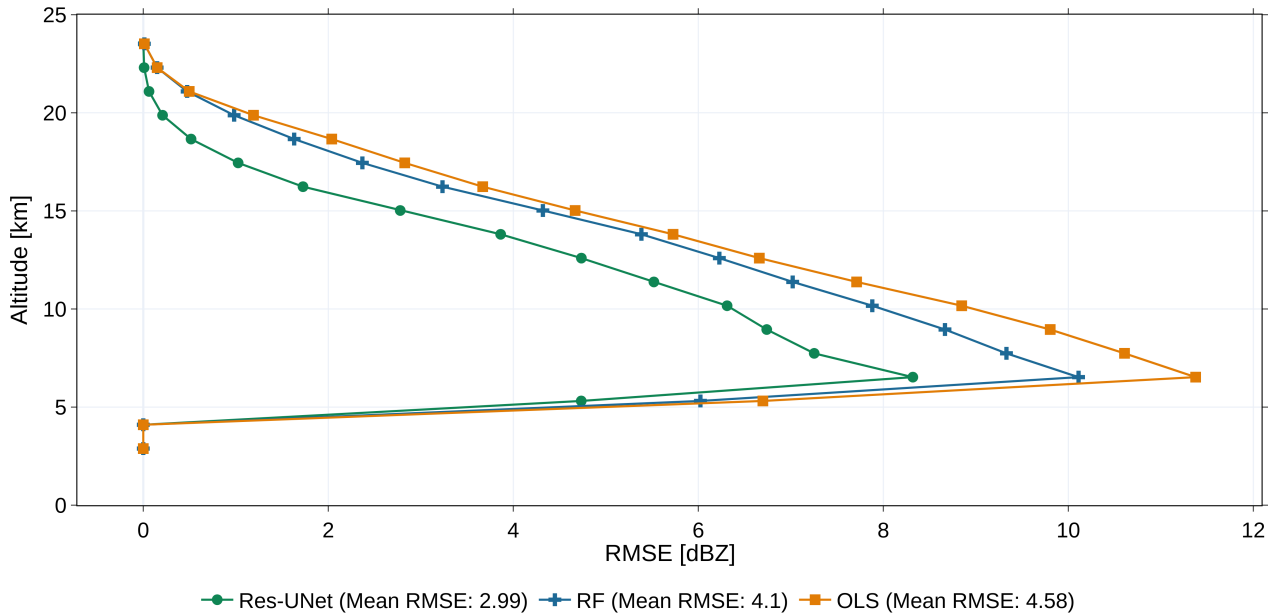
### 3.2 Height-dependent model performance

We analyze the model error (RMSE) along the vertical cloud column. For all models, we calculate the mean RMSE on the test dataset between 2.4–24 km. The results point out an overall lower RMSE for the Res-UNet reconstructs the clouds along the original track more adequately with a RMSE between than for the OLS and RF (Fig. 4). The mean RMSE varies between 2.99 dBZ for the Res-UNet, 4.1 –6.9 dBZ (RF), or 4.58 dBZ (OLS). On a dBZ scale between -25–20 dBZ, this is equivalent to an error of 10.1 % (OLS), 9.1 % (RF), or 6.6 % (Res-UNet). Between 2.4–5 km, the RMSE is 0. This is due to the lack of CloudSat observations after filtering noisy pixels (Fig. 4). Especially for clouds with a less uniform shape, it represents the small-scale variability with higher accuracy. In the core regions of the cloud, the underestimation of high reflectivities is demonstrated. A denominational structure within each cloud is apparent (2, a). Between 5–7 km, the RMSE increases to up to 8 dBZ for the Res-UNet, 10 dBZ for the RF and OLS. Contrasting, the output of the Res-UNet pictures more interconnected and smooth features. The OLS and RF fail to predict shallow clouds at high altitudes and complex structures of multi-layered clouds. Here, and 12 dBZ for the OLS (Fig. 4). In higher altitudes, the performance of all models improves. The RMSE decreases to 4 dBZ (5.7 dBZ, 6 dBZ) for the Res-UNet shows more robust results leading to a more accurate reconstruction of the CloudSat data.

Due to the applied quality flag, few clouds are detected below 5 km, thus, no RMSE is calculated here (RF, OLS) at 15 km and reaches its minimum at 22 km (24 km for OLS and RF). Above 15 km, we have few CloudSat observations > 15 dBZ (Fig. 2). After a stage of adjustment, more pixels pass the quality criterion above this level. An enhanced RMSE of 8 dBZ for the Res-UNet accompanies this sudden augmentation of available data points. Further increasing altitudes correspond to a decreasing RMSE. More uniform clouds above 15 km, a). We observe a lower model error (Fig. 4) and reduced difference between the distributions (Fig. 3) in these height levels for all three models. The improved performance can be led back to the superior number of background reflectivities or the presence of more uniform clouds, like extended tropical cirrus, are easier to predict. In turn, this leads to a lower model uncertainty (Fig. 2, Fig. 3). That said, the results display a trade-off between generating noise-free images and minimizing the amount of skipped data points. While the model accurately identifies single-layer clouds and their. Over all height levels, the Res-UNet has the lowest RMSE of the three models. Compared to the OLS (RF), the mean RMSE of the Res-UNet is reduced by 34,8 % (27,1 %).

Figure 5 shows the predicted and observed reflectivity along the radar transect for four randomly chosen samples. For all models, the reconstructed cloud signal is predicted at the right horizontal location along the radar track, it misses the sharp edges of multi-layer clouds, especially in mid-altitudes. Most clear-sky situations are recognized with an almost noise-free background cross section. Clear-sky situations of -25 dBZ are recognized without noise. The cross sections in Figure 5 (a) are created using processed CloudSat reflectivities with a resolution of 0.03°. Although the radar pixels lose some sharp contrasts after the downsampling, we observe a higher blurriness for the predictions. The edges of individual clouds smear out for all three models. Even though all transects were labelled as cloudy, we see a high percentage of background pixels.

For the Res-UNet, we observe a RMSE between 3.3 and 8.2 dBZ. The overall shape and increased intensification towards the cloud's core follow the radar, even though edges are blurred, and peak reflectivities remain underestimated (Fig. 4)–5, b).



Reconstructing the vertical radar track along the horizontal diagonal XY-axis. Values lower than -25 dBZ are displayed transparent. For each sample (I)–(IV) the reflectivity is compared between the processed CloudSat CPR track and the predictions of the Res-UNet, the OLS, and the RF.

**Figure 4.** Height dependent RMSE for every height bin and the mean RMSE for all models calculated on the test dataset ( $n = 1500$ ).

This issue is reflected within the reflectivity distribution of the DL model (Fig. 2, b). While the Res-UNet accurately identifies single-layer clouds, it misses sharp edges of multi-layer clouds, especially in mid-altitudes. Clouds over multiple height levels are blurry and show a reduced small-scale accuracy in the vertical dimension (Fig. 5, III). The lower height levels of multi-layer clouds are only partly represented (Fig. 5, II, IV). Instead, we observe a simplification of these cloud layers.

For the OLS and the RF, the underestimation of the cloud core reflectivities resembles the Res-UNet (Fig. 5, II, III). All four examples show a higher RMSE for the OLS and RF than for the Res-UNet (Fig. 5, c, d). The difference varies between 0.1 (I) and 2.7 (IV) dBZ. While the error is predominantly similar for all three models, the shape of the predicted clouds differs (I, III). The OLS (RF) fails to accurately reconstruct the vertical extent in all transects. Instead, the reflectivity is uniform along the cloud column. We see a continuous cloud signal between 5–15 km (Fig. 5, c). Contrasting, the Res-UNet predicts the vertical variability more precisely (Fig. 5, b). While the 2D profiles of the Res-UNet are smooth, the RF and OLS lead to a fragmented structure with a high value variability between the single pixels of the transect (I, IV). The examples show an inaccurate reconstruction of shallow clouds and multi-layer clouds for the OLS and RF.

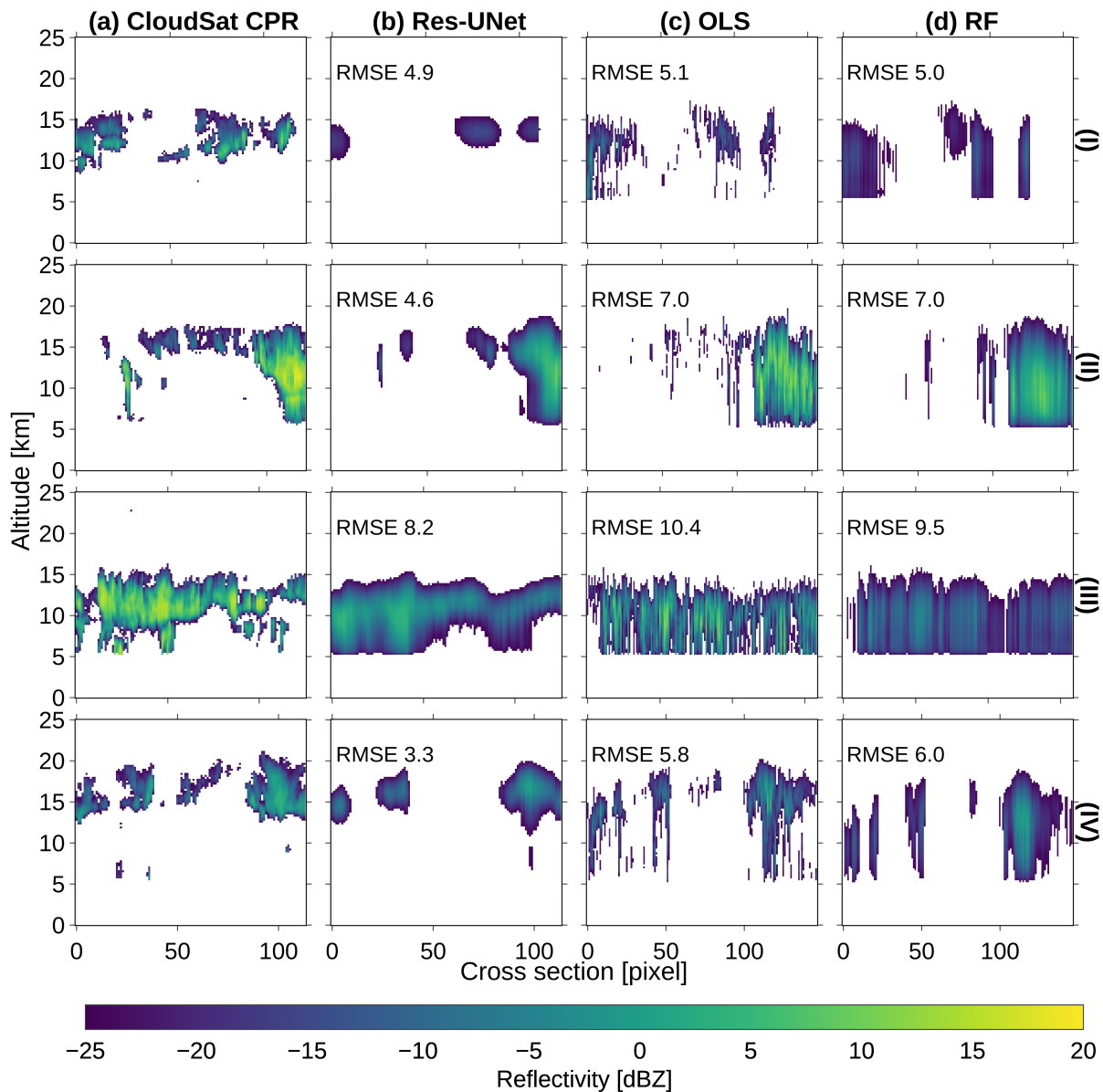


**Figure 5.** Reconstructing the radar cross section for four random examples of the test dataset ( $n = 1500$ ). Values  $\leq -25$  dBZ are displayed transparent. We compare the reflectivity between the processed CloudSat cross sections (a) and the predictions of the Res-UNet (b), the OLS (c), and the RF (d) for each transect (I–IV). The RMSE describes the error between the CloudSat data and the predicted profile.

### 3.3 Implications and sample applications

#### 420 3.3 Geographic analysis of the 3D cloud tomography

~~The trained~~ With the trained Res-UNet was used to evaluate the pixel-based vertical columns and predict clouds on the whole image domain. Results contain a 3D representation within each output image along 90 height bins. Even though observational data is missing for most pixels, smooth cloud structures can be derived in different proximity to the track (Fig. 5). ~~These 3D images are the basis to create comprehensive predictions,~~ we predict clouds on the MSG SEVIRI ~~FD~~ AOI. Since the network ~~was trained using VIS channels, we cannot provide an accurate representation of the nocturnal cloud field. An exemplary 3D cloud tomography is predicted for 06 May 2016, 13:00 UTC.~~ For that purpose, the satellite scene was divided into small subsets of overlapping 128 x 128 pixel images as described in Section 2.3.2. After feeding each subset into the network, the output ~~samples~~ tiles of 90 x 100 x 100 pixels were merged into a FD scene of 90 x 2400 x 2400 pixels for the whole AOI. ~~The results of the column's maximum reflectivity demonstrate~~ (Fig. 6, a).

430 The results contain a 3D cloud field along 90 height bins between 2.4–24 km. As shown in Figure 6 (a), the top-view on the maximum reflectivity per cloud column demonstrates the absence of hard borders ~~but~~ between single prediction tiles. Even though CloudSat data is only available at the radar transects, we can extrapolate smooth cloud structures on the FD. ~~The example tiles (b)–(d) point out a fluent transition between image edges that enable the identification of large-scale cloud patterns. The diversity of cloud types depicted within the samples in Figure 5 illustrates the transferability of the approach to~~ different locations and their environmental conditions. High clouds, convective complexes, and isolated cores are represented as smooth structures edges of single prediction tiles (Fig. 6). Each example spans a horizontal extent of  $> 2.5^\circ$  (100 x 100 pixels) to demonstrate the absence of artifacts between the tiles. High reaching convective complexes (b) and large-scale structures (c, d) are extrapolated at the FD scale regardless their location. Even though the overall reflectivity is underestimated, low-level and multi-layer clouds are displayed as contiguous entities.

440 ~~Following~~ We visualize the mean RMSE between 60 °N and 60 °S to investigate zonal variations for the test dataset. The geographic analysis is used to evaluate the reliability of the 3D representation, ~~the CTH was derived from the CloudSat reflectivities and the~~ cloud tomography. The RMSE shows a high latitudinal variability. At 30–50 °N, we observe the highest RMSE of 6–7 dBZ (Fig. 7, a). The RMSE at mid-latitudes on the southern hemisphere is lower than at the northern hemisphere. Nevertheless, the lowest RMSE is achieved in the tropics between 20 °N–20 °S. We analyze the RMSE in relation to the ~~number of image-profile pairs originating the matching scheme in Section 2.1.3. Most image-profile pairs are located around the equator and the mid-latitudes (Fig. 7, b). Few pairs are matched around 10 °N and 30 °S. Regions in the mid-latitudes have the highest RMSE and the highest number of observations. In the tropics, the RMSE is lower. Here, we obtain a high amount of image-profile pairs from the matching scheme. The predicted cloud field points out a high geographic variability of the RMSE. We observe a higher RMSE for the northern than for the southern hemisphere. Clouds in the subtropics are more accurately~~ represented than clouds in high latitudes. At the same time, we lack observations here. The analysis emphasizes the importance of the geographic location on the model predictions as well as the influence of the CloudSat orbit.

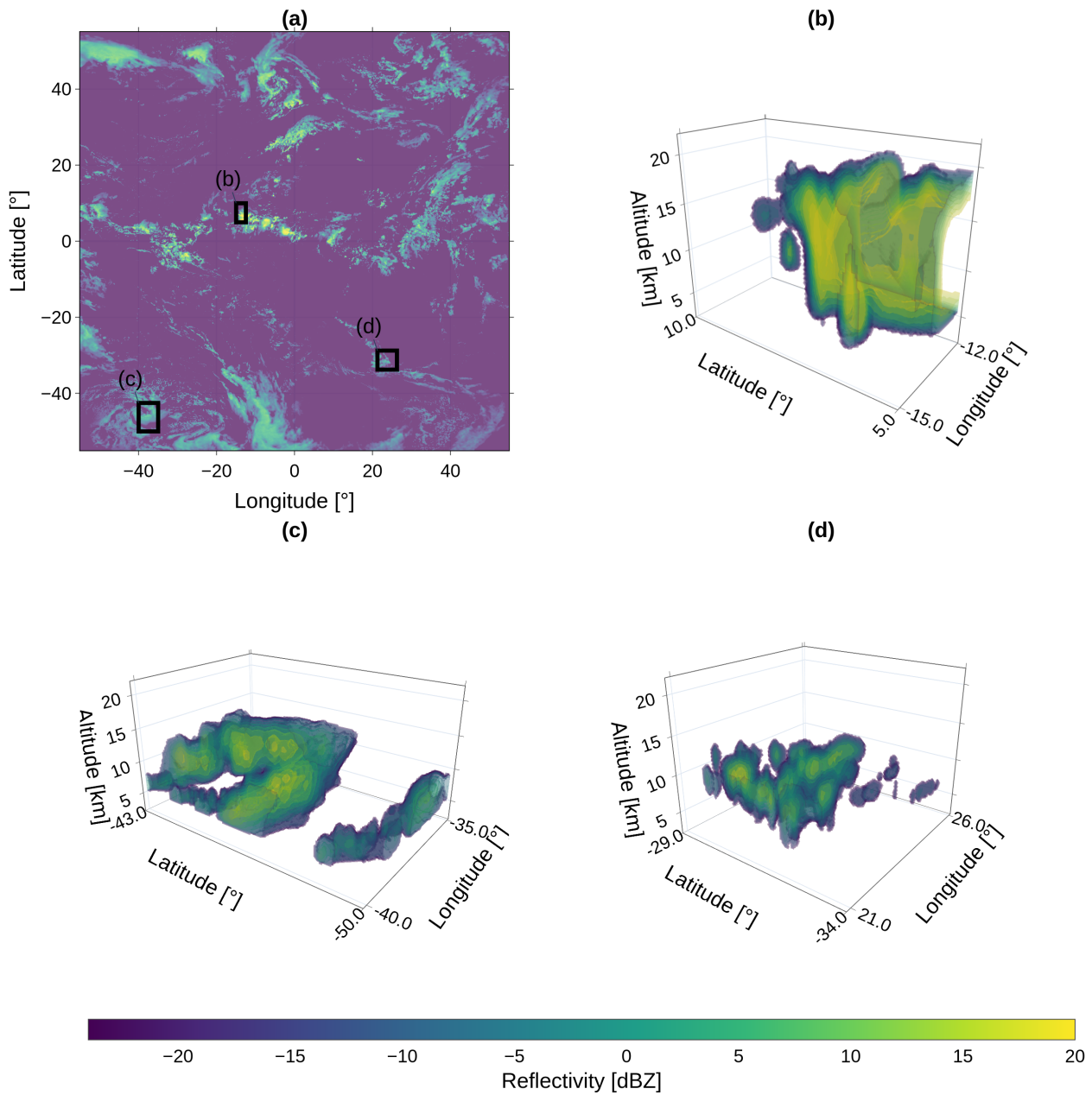


**Figure 6.** Prediction of 3D cloud structures from the Res-UNet along the FD MSG SEVIRI domain with a top-view on the maximum cloud column reflectivity for each pixel on 06 May 2016, 13:00 UTC (a). The detailed views in (b), (c), and (d) span several tiles of 100 x 100 pixels (2.5 ° on the geographic grid) to point out the absence of artifacts between predictions.

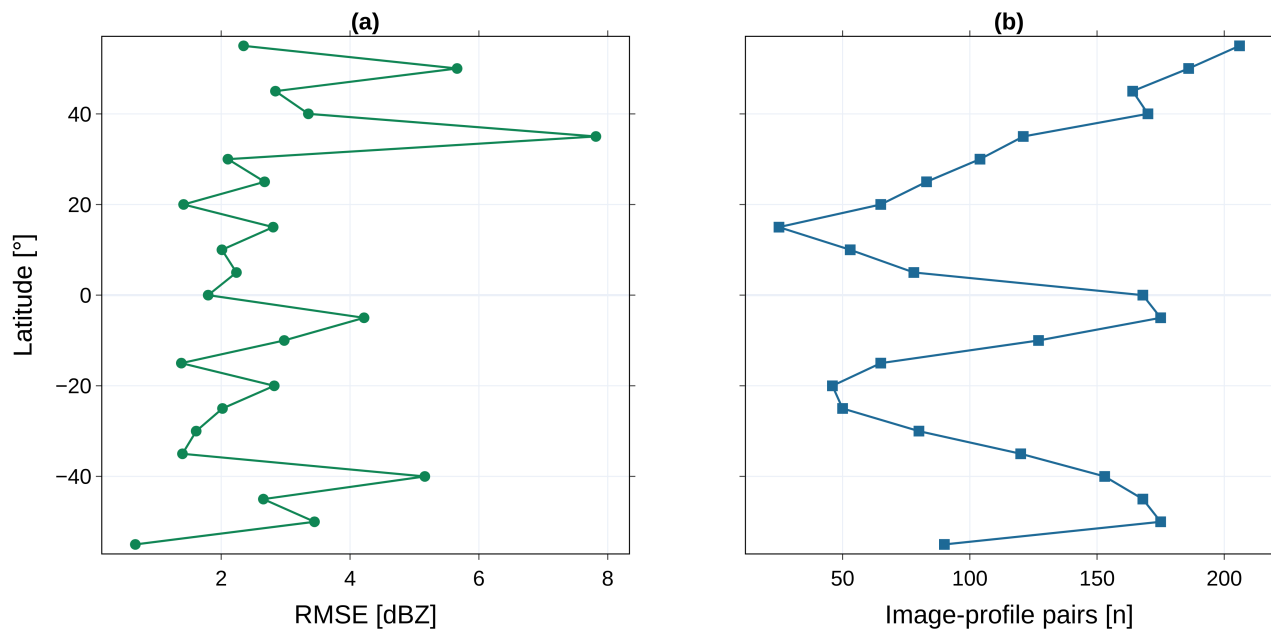


**Figure 7.** Zonal RMSE of the Res-UNet (a) and number of matched image-profile pairs used for model evaluation (b) for latitudes between 60 °N and 60 °S (n = 1500).

### 3.4 Comparison of the predicted CTH

To evaluate the quality of the Res-UNet predictions. Considering the available data points for the calculated CTH, predicted images surpass the radar observations by 10.000. Comparing the distributions in Figure 6 shows lower reflectivities for predicted than for observational data. Again, predictions, we compare the reflectivity distribution between CloudSat and the Res-UNet predictions. In a second step, we calculate the CTH on the test dataset. The reflectivities in Figure 8 (a) are provided in logarithmic scale due to the high proportion of background values cloud-free pixels around -25 dBZ rests upon the imbalance within the radar data. Both datasets provide more similar results concerning the frequencies above -15 dBZ. This distinction emphasizes an overall surplus of background values in the FD prediction (Fig. 8 a, c). Values < -15 dBZ are visualized with a grey background. They lie below the threshold used to determine a cloud signal for the calculation of the CTH (Sect. 2.3.3). The distribution of CloudSat and predicted reflectivities is similar for up to -10 dBZ. For higher reflectivities, the distributions diverge. As demonstrated in Figure 2, the network fails to accurately reconstruct high reflectivities. The difference increases for reflectivities > 0 dBZ. Both reflectivity distributions are dominated by cloud-free pixels of -25 dBZ 8 (c). The comparison points out the importance on the background value for the whole distribution. For values > -15 dBZ, the difference between the distributions decreases. The shift of the distribution is reflected in the CTH in Figure 8 (b). Both datasets display a maximum CTH at up to 7 km height. This first peak is overestimated by the model. The absence of a second peak around 12–15 km height is reflected within the normalized difference. Here, the model shifts towards lower altitudes than the observational data (Fig. 6) underestimated by the Res-UNet. The difference between the predicted CTH is reflected within Figure 8 (d). The mismatch between the two peaks is about the same size. The underestimated second peak can be traced back to high clouds with a low optical thickness, which is sometimes not well recognized, especially in the visible channels of MSG SEVIRI. These channels are identified as essential information providers for the ML algorithm, and therefore those high clouds are also underestimated in the derived radar reflectivities.

Although the total led back to the inaccuracy of the predicted reflectivities. The Res-UNet overestimates reflectivities < -15 dBZ at all height levels up to 15 km. It misses high reflectivities responsible for the peak of the CTH at 12–15 km (Fig. 3, b). Instead, we see an overall surplus of background values in the FD prediction.

Calculating the CTH on the FD predictions substantially increases the amount of available data points compared to the CloudSat data. Predicted images surpass the radar observations by a factor of 10000. We use the 3D cloud tomography to derive the FD CTH on the test dataset. For each time step, we calculate the CTH on the FD and aggregate the results to a monthly mean. These values are compared to the CLAAS-V002E1 product with a resolution of 0.05 ° (Finkensieper et al., 2020). The predicted CTH has a resolution of 0.03 °. Due to this mismatch, our predictions show more fragmented structures (Sect. 2.3.3). Although the small-scale accuracy is improvable, derived data and deducted parameters allow an expedient the results allow an investigation of regional differences. Comparing the model output and the CTH from the CLAAS-V002E1 product (Finkensieper et al., 2020) on the large scale. The analysis reveals an overall high agreement. Regional differences arise around the equator and mid-to-high latitudes. Regarding the first, the mid- to high-latitudes (Fig. 9). In mid-latitudes, the CTH over water bodies is overestimated in the southern hemisphere and underestimated in the northern hemisphere. These differences can

be led back to an increased RMSE in these regions (Fig. 7). In contrast, a low RMSE in the subtropics increases the accuracy of the predicted CTH. The model is biased toward predicting lower clouds. ~~In the latter regions, they appear too intense, especially over water bodies of the southern~~ than the observational data. Overall, the Res-UNet overestimates the occurrence of clouds in 6-8 km while underestimating high clouds (Fig. 8, b).

490 This issue is reflected within Figure 10. Here, we visualize the geographic distribution of the CTH difference (Fig. 10, a). The mean difference over all pixels accounts for 1.28 km. While the data show an overall agreement, the pixel-wise difference rises to a maximum of 10 km. This applies especially to regions in the subtropics. We observe an underestimation of the predicted CTH over land. Above the Atlantic ocean, especially in the tropics, the predictions are too high. The highest difference occurs in subtropics on the northern hemisphere (Fig. 7). ~~Unlike most satellite-based procedures, the CTH is derived without integrating additional data, such as vertical temperature profiles from e. g., model forecast or re-analysis data. This simplification reduces the workload for users and the co-dependence of corresponding data. Therefore, the approach offers added value in terms of a more efficient investigation of cloud-related processes.~~ 10, b). At 20 °N, the mean difference accounts for 5 km. Around the tropics and mid-latitudes, both datasets are in higher agreement. The distribution of the CTH difference is inversely proportional to the amount of matched image-profile pairs (Fig. 7, b). The CTH difference decreases with an increasing amount of observational data from CloudSat. This applies to predictions over land and sea. Since we lack ground truth in the subtropics, the performance of the predictions decreases. The geographical differences are only partly in accordance to the distribution of the RMSE (Fig. 7, a). While the RMSE is lower in northern subtropics, the error of the predicted CTH reaches its peak (Fig. 10, b). The RMSE alone does not appear to be a suitable measure to define the reliability of the predicted reflectivity on the FD. This is due to influence of the skewed reflectivity distribution on the RMSE and its geographic variability.

505 ~~Prediction of 3D cloud structures for the FD MSG SEVIRI domain with a top-view on the maximum cloud column reflectivity for each pixel on 06 May 2016, 13:00 UTC (a). The detailed views in (b), (c), and (d) show the cloud tomography at different locations of the FD~~ Even though the comparison of the CTH points out regional differences, the predictions can be used to represent the CTH pattern on the FD. The CLAAS-V002E1 data is computed using the MSG SEVIRI satellite channels as well as derived products and additional data. Each of them bring their own bias, potentially multiplying their effects on the final CTH. In contrast, our CTH is based only on the predicted reflectivity. In that way, we can minimize the influence of additional data sources.



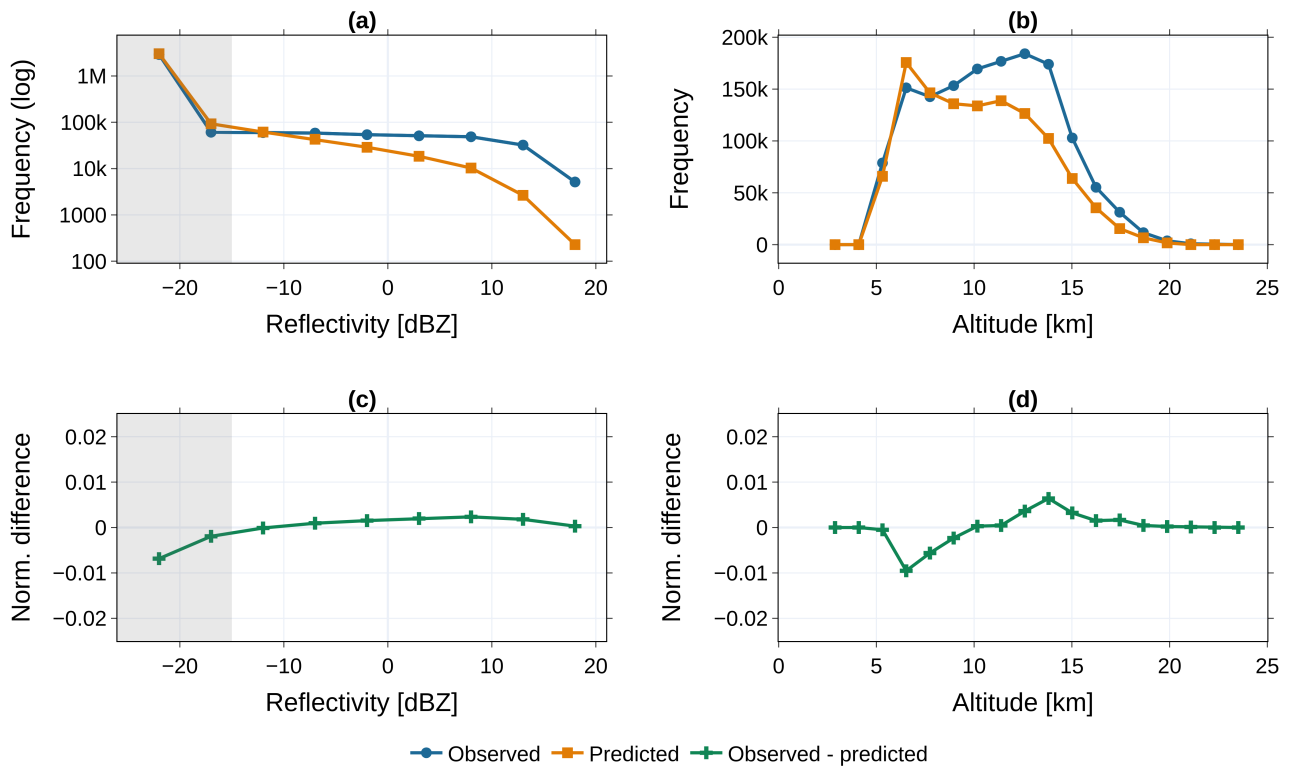


**Figure 8.** Comparing the FD-reflectivity distribution of reflectivities and CTH the derived from CTH for CloudSat and the model Res-UNet predictions. Data is calculated on the test dataset and aggregated for May, 2016 to a monthly mean ( $n = 1500$ ). The upper row frequencies (a) and (b) display the dBZ and computed CTH for observed and predicted data. Lower row images (c) and their normalized (d) show the difference between the observed and predicted data. Grey areas lie on the plots (a) and (c) contain reflectivities below the threshold of -15 dBZ applied for the CTH analysis. Lower row images (e) and (d) picture the frequency of

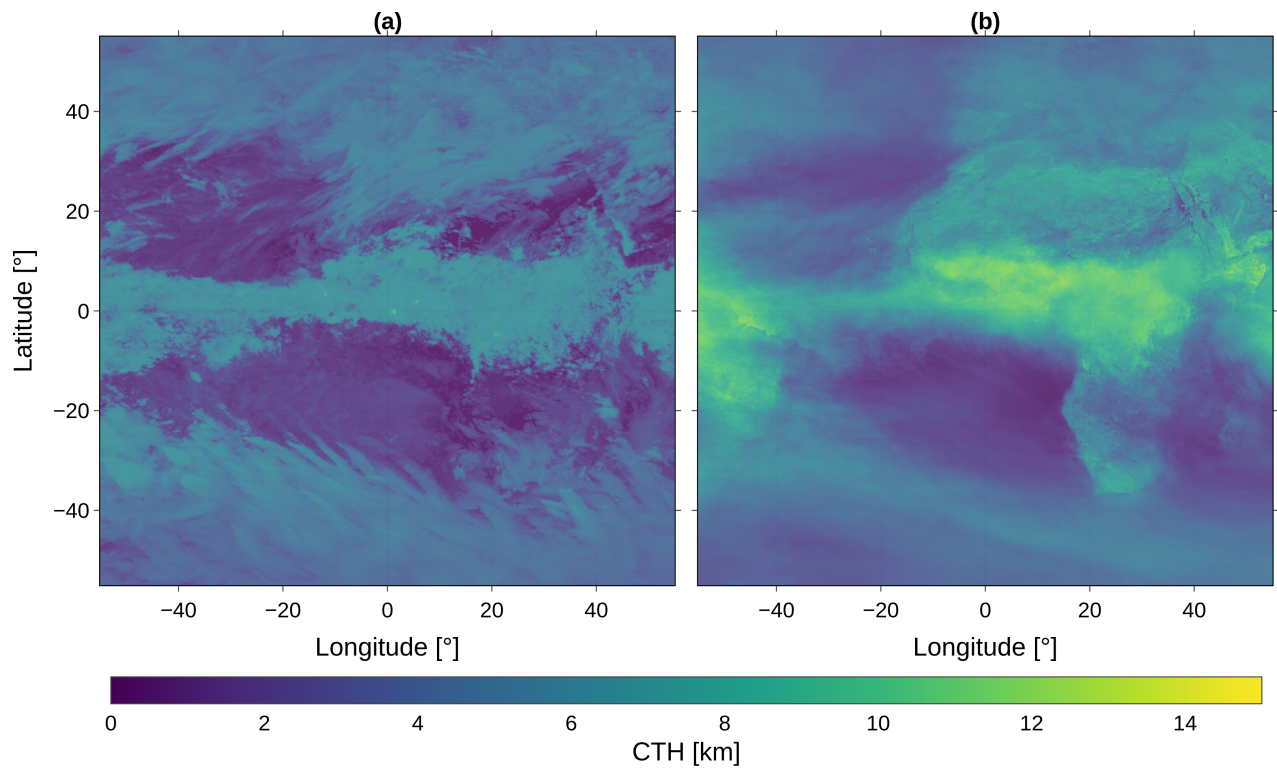


**Figure 9.** Monthly aggregation for the derived CTH per height level (for observations above -15 dBZ) alongside the normalized difference between 5-24 km height May 2016 (a) compared to CLAAS-V002E1 CTO (b).

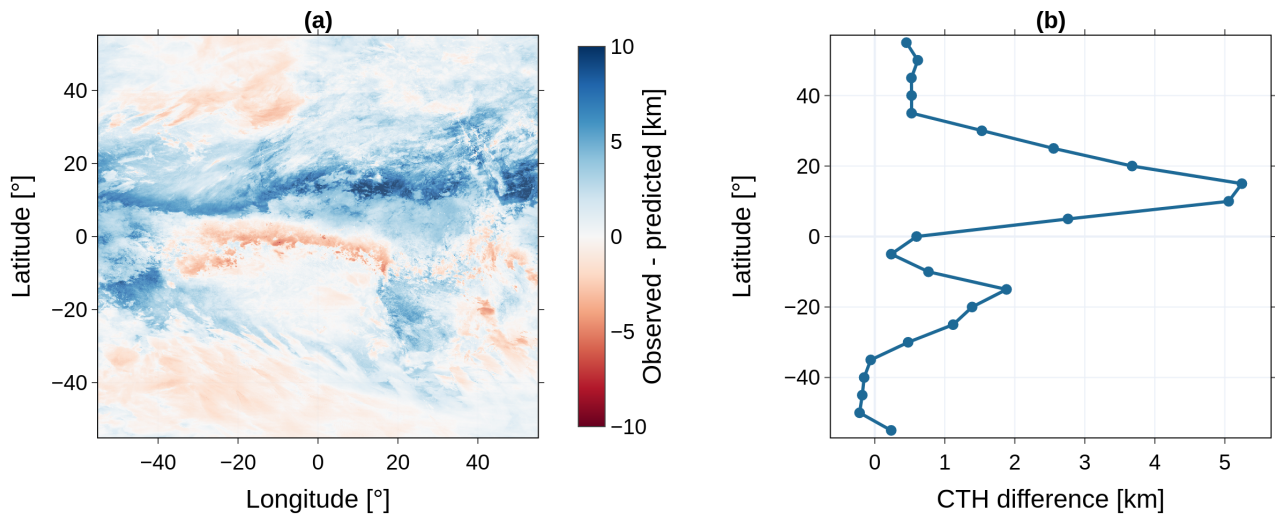


**Figure 10.** Aggregated CTH derived from the Res-UNet (a) and from the [Difference between](#) CLAAS-V002E1 CTO [product](#) (b) [and the](#) [computed CTH](#) for May 7, 2016. [Plot \(a\)](#) shows the geographic distribution on the FD. [\(b\)](#) the zonal error.

## 4 Discussion

In contrast to established ML methods like RF which need a cumbersome selection of predictor variables, the network in this study learns directly from the data (Kühnlein et al., 2014; Leinonen et al., 2019). That said, the DL approach reduces the time spent on processing and the user-generated bias (Jeppesen et al., 2019; Jiao et al., 2020). Standard DL models often use The Res-UNet makes predictions based on the satellite channels, preserving the spatial details and global context during training (Wang et al., 2022). The error of the model varies depending on cloud structure within the radar cross-section. Compared to pixel-based approaches like OLS, the Res-UNet better reconstructs the pixel connectivity. The OLS and RF operate on 1D cloud columns. This limits their ability to extrapolate cloud information to a larger scale, resulting in fragmented reconstructions (Fig. 5, c, d). While the RMSE and the reflectivity distribution are similar across all models, only the Res-UNet predicts a contiguous radar cross-section. Choosing a DL framework eliminates the need for prior predictor variable selection (Kühnlein et al., 2014; Leinonen et al., 2019). This can reduce the user bias in the input data (Jeppesen et al., 2019; Jiao et al., 2020).

The Res-UNet shows a 30 % improvement in the mean RMSE (Fig. 4). We could potentially further enhance the model performance by utilizing a more complex architecture. Our input data differs from typical gray-scale or RGB images (Dröner et al., 2018). In contrast, the input data in our study consists of multiple satellite channels. That is why, as it comprises multiple input channels and results in a 3D output (Dröner et al., 2018). Given the demands of our data and resource constraints, we adapted a standard UNet architecture rather than using a pre-trained model is restrained by expensive modifications (Amato et al., 2020). To evaluate the feasibility of the approach, we test a minimal architecture for transferring the 2D resolved satellite data to a 3D perspective (Amato et al., 2020). Selecting the RMSE as a loss function can increase the blurriness in the results, particularly as model bias grows (Mathieu et al., 2016). This issue becomes apparent as all models struggle to predict high reflectivities (Fig. 2, b-d). The predictions are influenced by an imbalance within the CloudSat data, with the distribution of all models skewed toward low reflectivities. A resolution mismatch between CloudSat and MSG SEVIRI exacerbates this imbalance, causing peak reflectivities to blur out (Fig. 5, b-d).

While Hilburn et al. (2020) were able to reconstruct the radar signal Our study covers a large-scale AOI spanning  $60^\circ$  in all directions. In contrast to studies of Leinonen et al. (2019) or Hilburn et al. (2020), we incorporate a diverse landscape into our training. While Hilburn et al. (2020) focused on radar signal reconstruction over the USA, they are limited to a planar representation and leave out cloud development using land-based radar, Leinonen et al. (2019) concentrated on radar cross-section prediction over the sea surface. Contrasting their and others work, our study integrates a heterogeneous landscape into the training routine (Leinonen et al., 2019; Le Goff et al., 2017; Hilburn et al., 2020; Forster et al., 2021). The latitude and topography are highly influential for. In our study, we match image-profile pairs over land and sea to achieve model invariance to the topography. The performance of our Res-UNet is similar to their results. Nevertheless, we observe regional difference, especially for the CTH. We use a geographical analysis to highlight the importance of the topography and land-sea distribution and their impact on cloud microphysics (Wang et al., 2023). Nonetheless, defining those variables as additional predictors has a negligible effect on the model performance. Instead, the network performs equally well over land and ocean bodies capturing the shape of convective and shallow clouds. Predictions at nighttime are limited

We emphasize the influence of the geographic location and the CloudSat orbit, particularly in regions farther from the equator, where sensor accuracy diminishes (Fig. 7). Currently, we estimate the model error to be mainly influenced by the data imbalance and chosen loss function. In the future, addressing the cloud parallax shift in high-angle satellite observations could enhance the results by a more accurate image-profile matching (Bielński, 2020). The most accurate predictions fall between 25 °N and 25 °S (Fig. 7), while mid- and high-latitudes exhibit a higher RMSE. This is likely due to the land-sea distribution and connected cloud patterns. Over ocean bodies, the model overestimates the reflectivity (Fig. 10, a). Using the water vapor channels could lead to this distortion. Improved predictions are evident over the southern hemisphere. Since CloudSat operates on a sun-synchronous orbit, it misses diurnal variations in each region (Sect. 2.1.2). In this study, we only derive daytime predictions. This is due to the influence of solar radiation in ~~the channels located within wavelengths of the visible spectrum~~ (Hilburn et al., 2020; Jeppesen et al., 2019). ~~Leaving out the affected channels downgrades the overall performance. While the results imply a high agreement between observations and predictions, distortions are possible. Since the satellite data deliver only information on the uppermost layer~~ visible spectrum (VIS) channels (Hilburn et al., 2020; Jeppesen et al., 2019). Additional distortions may arise from VIS channels, ~~the incoming signal could originate from any surface with an enhanced as satellite images only represent the uppermost cloud layer. Depending on the location, they can be highly influenced by the~~ surface albedo (Dröchner et al., 2018).

~~The Res-UNet in this study generates its predictions with the influence of the neighboring pixels along the image domain. In contrast to pixel-based DL methods like the CNN or CGAN, the Res-UNet utilizes a larger receptive field preserving the spatial dimensionality and global context information during the training routine (Wang et al., 2022). Thus, it receives a more accurate spatial connectivity between the pixels and following, the clouds within the image. While the OLS and RF solely get information on the reflectivities along a single cloud column, the Res-UNet enables an interpolation towards an FD perspective. While the CGAN was restrictively trained over sea surfaces, the influence of the variability of the topography beneath needs to be included (Wang et al., 2023). The restoration of the original track is~~ Training a model without the VIS channels can help to achieve predictions independent of the daytime. Reducing the extent of the AOI can mitigate the geographic performance differences but limits the applicability of the network. Training regional models and adjusting the loss function and model architectures offer potential solutions to improve the results of the 3D cloud tomography.

The reconstructed CloudSat cross sections are comparable to results achieved by Leinonen et al. (2019) ~~and Wang et al. (2023)~~. ~~The~~. For both studies, the RMSE varies between 0–1 dBZ for cloud-free samples, 3–7 dBZ for more uniform clouds, and more than 10 dBZ for multi-layer clouds (Leinonen et al., 2019). ~~All networks struggle to depict. A common limitation is accurately representing multi-layer structures accurately~~ clouds. Using the satellite channels to derive these information may be limited (Schmetz et al., 2002; Thies and Bendix, 2011). High reflectivities tend to be underestimated due to noise near the ground (Stephens et al., 2008). ~~Due to the sensor limitations of CloudSat, few signals close to the ground are received (Stephens et al., 2008). In consequence, predictions at low altitudes are error-prone. This issue is reflected within the normalized differences between observed and predicted reflectivities~~ To mitigate this, we exclude affected height levels, but this results in incomplete model predictions between 0–5 km (Fig. 2). Similar results are achieved by Leinonen et al. (2019) where falsely estimated reflectivities appear in similar dBZ regions up to 12 km height. In both cases, an underestimation of high reflectivities

is predominant. Since the input data of Reducing noise is crucial for improving the performance of DL applications in remote sensing (Enitan and Ilesanmi, 2021). Our results are significantly influenced by the resolution difference between CloudSat and MSG SEVIRI, as well as the choice of the CGAN-originate loss function (Sect. 2.1.3). The aggregation of CloudSat pixels blurs contrast within individual clouds (Fig. 5, a), which is further reflected in the increased RMSE. In contrast, Leinonen et al. (2019) use data from the MODIS satellite, it (Zantedeschi et al., 2022). It has a higher native spatial resolution than the MSG SEVIRI data enabling allowing for sharper predictions along the track. On the other hand, the mismatch between CloudSat and MSG SEVIRI requires an aggregation of each radar pixel leading to reduced contrasts and blurry edges within individual clouds. Nevertheless radar transect. However, polar-orbiting satellites like MODIS lack the spatio-temporal coverage compared to of geostationary satellites (Dubovik et al., 2021). In their study, Wang et al. (2023) derive 24000 training samples for matching CloudSat and MODIS over six years. By using MSG SEVIRI data, the amount we amplify the volume of training data substantially increases. Matching MODIS with CloudSat accounts for about 24,000 training samples for six years (Wang et al., 2023). This study extracted about 30,000 training samples for only one year, equaling. We have extracted approximately 30000 training samples from one year of satellite data, which results in a ratio of about 1:7 for the whole period.

7. A Currently, a compromise on the resolution is necessary to obtain predictions on the FD for Europe and Africa. However, newly emerging instruments offer an enticing prospect to tackle this information loss. The recently launched satellite promising new instruments are emerging. While data from comparable sources like the GOES-R series and the Himawari 8/9 satellites already offer a 1 km resolution, the recently launched Meteosat Third Generation by EUMETSAT (Holmlund et al., 2021) provides data in a resolution of 1 km. This sensor allows a more accurate satellite by EUMETSAT allows to close the gap and enables a more precise representation of individual clouds. While the approach is currently restricted to a domain of 60 (Holmlund et al., 2021). Although our approach currently focuses on a region centered around  $0^\circ$  in all directions, assimilating related geostationary satellites helps to achieve global coverage. Consequently, this model can be used to close current gaps in the longitude, we can apply the same framework to other geostationary satellites, potentially achieving global 3D representation of clouds, leading to a seamless coverage of the vertical column along the troposphere for the first time cloud coverage throughout the troposphere. The predicted cloud field can be valuable for time series analysis, enabling the tracking of clouds in four dimensions across space and time. Our results facilitate the identification of large-scale cloud patterns. They offer various applications, such as analyzing cloud organizational structures, pinpointing lightning locations, or conducting precipitation onset analyses. While we use CloudSat radar data as our ground truth, this approach can be adapted to other 2D transect data sources, such as aerosol measurements.

## 610 5 Conclusions

With the help of a neural network, this study demonstrates we demonstrate for the first time the potential to infer a comprehensive 3D perspective of radar reflectivities from 2D geostationary satellite data for the first time images. While former studies are restricted to a regional extent or the flight path of the ground truth instrument, this approach provides a flexible

~~and landscape-independent~~ were confined to a smaller region or the reconstruction of the 2D radar transect, we provide a  
615 framework to model the ~~cloud signal with~~ 3D cloud field in a high spatio-temporal resolution. ~~Since it is independent of~~  
~~external or interconnected data sources, the bias within the data is reduced~~ The study is focused over Africa and Europe, but  
~~the approach can be used to predict the radar reflectivity on a global scale. Using only the predicted reflectivity, we derive~~  
~~the CTH without external data sources~~. Overall, the approach ~~leads to an accurate representation of multi-scale dynamics~~  
~~accurately reconstructs cloud structures~~ in varying environmental conditions ~~on the FD~~. Although the results are affected by  
620 sensor-specific ~~and technical~~ limitations, a vast potential for applications in ~~the field of weather and climate~~ atmospheric and  
~~climate sciences~~ is apparent. With steadily growing data and the emergence of improved instruments, the results can close the  
consisting global data gap. ~~We emphasize the benefit to extrapolate a 3D cloud field~~, especially in ~~secluded regions and above~~  
~~the sea surface~~ remote oceanic regions. Future work will focus on extending the proposed network by data with an enhanced  
spatial and temporal resolution and investigating 3D cloud processes in proceeding applications.

**Table A1.** Hyperparameters and training parameters of the Res-UNet.

<u>Type</u>	<u>Parameter</u>	<u>Value</u>
Hyperparameters	<u>Depth</u>	<u>4</u>
	<u>Input channels</u>	<u>11</u>
	<u>Output channels</u>	<u>90</u>
	<u>Filter size</u>	<u>3 x 3</u>
	<u>Pooling size</u>	<u>2 x 2</u>
	<u>Dropout</u>	<u>0</u>
	<u>Activation function</u>	<u>ReLU</u>
Training parameters	<u>Number of epochs</u>	<u>50</u>
	<u>Batch size</u>	<u>4</u>
	<u>Input size</u>	<u>128 x 128</u>
	<u>Crop size</u>	<u>100 x 100</u>
	<u>Initial learning rate</u>	<u>0.001</u>
	<u>LR scheduler (factor)</u>	<u>0.1</u>
	<u>Optimizer</u>	<u>ADAM</u>
	<u>Weight decay</u>	<u>0.00001</u>
	<u>Loss function</u>	<u>RMSE</u>
	<u>Augmentation (horizontal flip)</u>	<u>Randomness = 50 %</u>

**Appendix B: Summary of trainable model parameters****Table B1.** Total number of the Res-UNet model parameters.

<u>Total number of trainable parameters</u>	<u>Estimated total size (MB)</u>
<u>1.893.328</u>	<u>194.27</u>



*Code and data availability.* The source code for the satellite data matching scheme and model framework are available upon request to the corresponding author and will be published with acceptance. Meteosat SEVIRI image data used in this study have been downloaded at <https://navigator.eumetsat.int/product/EO-:EUM:DAT:MSG:HRSEVIRI> (EUMETSAT Data Services, 2023). The level 2B-GEOPROF  
630 CloudSat data have been downloaded at <http://www.cloudsat.cira.colostate.edu/> (CloudSat Data Processing Center, 2023). The CLAAS-2.1 data were obtained from [https://doi.org/10.56-76/EUM\\_SAF\\_CM/CLAAS/V002](https://doi.org/10.56-76/EUM_SAF_CM/CLAAS/V002) (Finkensieper et al., 2020).

*Author contributions.* S.B and H.T. designed the study. S.B and S.N. developed the model code. S.B performed the modeling and visualization. S.B. and H.T. contributed to the model validation and analysis of cloud properties. S.B. and H.T. wrote the draft of the paper. All authors have read and agreed to the published version of the manuscript.

635 *Competing interests.* The authors declare that they have no conflict of interest.

*Acknowledgements.* The study is supported by the project “Big Data in Atmospheric Physics (BINARY)”, funded by the Carl Zeiss Foundation (grant P2018-02-003). We acknowledge the infrastructure provided by the Max Planck Graduate Center Mainz. We acknowledge EUMETSAT for providing access to the Meteosat SEVIRI image data. We acknowledge the Cooperative Institute for Research in the Atmosphere, CSU, for providing access to the CloudSat 2B-GEOPROF data. We acknowledge CM SAF for providing access to the CLAAS-2.1  
640 data. We thank P. Spichtinger for useful discussions and comments on the manuscript.

## References

- Amato, F., Guignard, F., Robert, S., and Kanevski, M.: A novel framework for spatio-temporal prediction of environmental data using deep learning, *Sci. Rep.*, 10, <https://doi.org/10.1038/s41598-020-79148-7>, 2020.
- Barker, H. W., Jerg, M. P., Wehr, T., Kato, S., Donovan, D. P., and Hogan, R. J.: A 3D cloud-construction algorithm for the EarthCARE  
645 satellite mission, *Q. J. R. Meteorol.*, 137, 1042–1058, <https://doi.org/10.1002/qj.824>, 2011.
- Bedka, K., Brunner, J., Dworak, R., Feltz, W., Otkin, J., and Greenwald, T.: Objective Satellite-Based Detection of Overshooting Tops Using Infrared Window Channel Brightness Temperature Gradients, *JAMC*, 49, 181–202, <https://doi.org/10.1175/2009JAMC2286.1>, 2010.
- Benas, N., Finkensieper, S., Stengel, M., van Zadelhoff, G.-J., Hanschmann, T., Hollmann, R., and Meirink, J. F.: The MSG-SEVIRI-based cloud property data record CLAAS-2, *ESSD*, 9, 415–434, <https://doi.org/10.5194/essd-9-415-2017>, 2017.
- 650 Bieliński, T.: A Parallax Shift Effect Correction Based on Cloud Height for Geostationary Satellites and Radar Observations, *Remote Sensing*, 12, <https://doi.org/10.3390/rs12030365>, 2020.
- Bocquet, M., Elbern, H., Eskes, H., Hirtl, M., Žabkar, R., Carmichael, G. R., Flemming, J., Inness, A., Pagowski, M., Pérez Camaño, J. L., Saide, P. E., San Jose, R., Sofiev, M., Vira, J., Baklanov, A., Carnevale, C., Grell, G., and Seigneur, C.: Data assimilation in atmospheric chemistry models: current status and future prospects for coupled chemistry meteorology models, *Atmos. Chem. Phys.*, 15, 5325–5358,  
655 <https://doi.org/10.5194/acp-15-5325-2015>, 2015.
- Bony, S., Stevens, B., Frierson, D. M. W., Jakob, C., Kageyama, M., Pincus, R., Shepherd, T. G., Sherwood, S. C., Siebesma, A. P., Sobel, A. H., Watanabe, M., and Webb, M. J.: Clouds, circulation and climate sensitivity, *Nat. Geosci.*, 8, 261–268, <https://doi.org/10.1038/ngeo2398>, 2015.
- Boulesteix, A.-L., Janitza, S., Kruppa, J., and König, I. R.: Overview of random forest methodology and practical guid-  
660 ance with emphasis on computational biology and bioinformatics, *WIREs Data Min. Knowl. Discov.*, 2, 493–507, <https://doi.org/https://doi.org/10.1002/widm.1072>, 2012.
- Breiman, L.: Random Forests, *Machine Learning*, 45, 5–32, <https://doi.org/10.1023/A:1010933404324>, 2001.
- Cao, K. and Zhang, X.: An Improved Res-UNet Model for Tree Species Classification Using Airborne High-Resolution Images, *Remote Sens.*, 12, <https://doi.org/10.3390/rs12071128>, 2020.
- 665 Chen, Y., Chen, G., Cui, C., Zhang, A., Wan, R., Zhou, S., Wang, D., and Fu, Y.: Retrieval of the vertical evolution of the cloud effective radius from the Chinese FY-4 (Feng Yun 4) next-generation geostationary satellites, *Atmospheric Chemistry and Physics*, 20, 1131–1145, <https://doi.org/10.5194/acp-20-1131-2020>, 2020.
- Cintineo, J. L., Pavolonis, M. J., Sieglaff, J. M., Wimmers, A., Brunner, J., and Bellon, W.: A Deep-Learning Model for Automated Detection of Intense Midlatitude Convection Using Geostationary Satellite Images, *Weather and Forecast.*, 35, 2567 – 2588,  
670 <https://doi.org/https://doi.org/10.1175/WAF-D-20-0028.1>, 2020.
- CloudSat Data Processing Center: Data Products, CloudSat DPC [data set], <https://www.cloudsat.cira.colostate.edu/data-products>, accessed: 2023-07-27, 2023.
- Denby, L.: Discovering the Importance of Mesoscale Cloud Organization Through Unsupervised Classification, *Geophys. Res. Lett.*, 47, <https://doi.org/10.1029/2019GL085190>, 2020.
- 675 Diakogiannis, F. I., Waldner, F., Caccetta, P., and Wu, C.: ResUNet-a: A deep learning framework for semantic segmentation of remotely sensed data, *ISPRS J. Photogramm. Remote Sens.*, 162, 94–114, <https://doi.org/10.1016/j.isprsjprs.2020.01.013>, 2020.

- Dixit, M., Chaurasia, K., and Kumar Mishra, V.: Dilated-ResUnet: A novel deep learning architecture for building extraction from medium resolution multi-spectral satellite imagery, *Expert Syst. Appl.*, 184, 115 530, <https://doi.org/10.1016/j.eswa.2021.115530>, 2021.
- 680 Drönner, J., Korfhage, N., Egli, S., Mühlhling, M., Thies, B., Bendix, J., Freisleben, B., and Seeger, B.: Fast Cloud Segmentation Using Convolutional Neural Networks, *Remote Sens.*, 10, 1782, <https://doi.org/10.3390/rs10111782>, 2018.
- Dubovik, O., Schuster, G., Xu, F., Hu, Y., Bösch, H., Landgraf, J., and Li, Z.: Grand Challenges in Satellite Remote Sensing, *Front. Remote Sens.*, 2, 619 818, <https://doi.org/10.3389/frsen.2021.619818>, 2021.
- Enitan, I. and Ilesanmi, T.: Methods for image denoising using convolutional neural network: a review, *Complex Intelligent Systems*, 7, <https://doi.org/10.1007/s40747-021-00428-4>, 2021.
- 685 EUMETSAT Data Services: High Rate SEVIRI Level 1.5 Image Data - MSG - 0 degree, <https://navigator.eumetsat.int/product/EO:EUM:DAT:MSG:HRSEVIRI>, accessed: 2023-07-27, 2023.
- Finkensieper, S., Meirink, J. F., van Zadelhoff, G.-J., Hanschmann, T., Benas, N., Stengel, M., Fuchs, P., Hollmann, R., Kaiser, J., and Werscheck, M.: CLAAS-2.1: CM SAF CLOUD property dAtAset using SEVIRI - Edition 2.1, [https://doi.org/10.5676/EUM\\_SAF\\_CM/CLAAS/V002\\_01](https://doi.org/10.5676/EUM_SAF_CM/CLAAS/V002_01), 2020.
- 690 Forster, L., Davis, A. B., Diner, D. J., and Mayer, B.: Toward Cloud Tomography from Space Using MISR and MODIS: Locating the “Veiled Core” in Opaque Convective Clouds, *J. Atmos. Sci.*, 78, 155–166, <https://doi.org/10.1175/JAS-D-19-0262.1>, 2021.
- Guillaume, A., Kahn, B. H., Yue, Q., Fetzer, E. J., Wong, S., Manion, G. J., Hua, H., and Wilson, B. D.: Horizontal and Vertical Scaling of Cloud Geometry Inferred from CloudSat Data, *J. Atmos. Sci.*, 75, 2187–2197, <https://doi.org/10.1175/JAS-D-17-0111.1>, 2018.
- Ham, S.-H., Kato, S., Barker, H. W., Rose, F. G., and Sun-Mack, S.: Improving the modelling of short-wave radiation through the use of a 3D scene construction algorithm, *Q. J. R. Meteorol.*, 141, 1870–1883, <https://doi.org/https://doi.org/10.1002/qj.2491>, 2015.
- 695 Han, L., Liang, H., Chen, H., Zhang, W., and Ge, Y.: Convective Precipitation Nowcasting Using U-Net Model, *IEEE Trans. Geosci. Remote Sens.*, 60, 1–8, <https://doi.org/10.1109/TGRS.2021.3100847>, 2022.
- Henken, C. C., Schmeits, M. J., Deneke, H., and Roebeling, R. A.: Using MSG-SEVIRI Cloud Physical Properties and Weather Radar Observations for the Detection of Cb/TCu Clouds, *Journal of Applied Meteorology and Climatology*, 50, 1587 – 1600, <https://doi.org/https://doi.org/10.1175/2011JAMC2601.1>, 2011.
- 700 Hilburn, K. A., Ebert-Uphoff, I., and Miller, S. D.: Development and Interpretation of a Neural-Network-Based Synthetic Radar Reflectivity Estimator Using GOES-R Satellite Observations, *J. Appl. Meteorol. Climatol.*, 60, 3–21, <https://doi.org/10.1175/JAMC-D-20-0084.1>, 2020.
- Holmlund, K., Grandell, J., Schmetz, J., Stuhlmann, R., Bojkov, B., Munro, R., Lekouara, M., Coppens, D., Viticchie, B., August, T., Theodore, B., Watts, P., Dobber, M., Fowler, G., Bojinski, S., Schmid, A., Salonen, K., Tjemkes, S., Aminou, D., and Blythe, P.: Meteosat Third Generation (MTG): Continuation and Innovation of Observations from Geostationary Orbit, *BAMS*, 102, 990–1015, <https://doi.org/10.1175/BAMS-D-19-0304.1>, 2021.
- 705 Hu, K., Zhang, D., and Xia, M.: CDUNet: Cloud Detection UNet for Remote Sensing Imagery, *Remote Sens.*, 13, <https://doi.org/10.3390/rs13224533>, 2021.
- 710 Huo, J., Lu, D., Duan, S., Bi, Y., and Liu, B.: Comparison of the cloud top heights retrieved from MODIS and AHI satellite data with ground-based Ka-band radar, *Atmos. Meas. Tech.*, 13, 1–11, <https://doi.org/10.5194/amt-13-1-2020>, 2020.
- Irrgang, C., Boers, N., Sonnewald, M., Barnes, E. A., Kadow, C., Staneva, J., and Saynisch-Wagner, J.: Towards neural Earth system modelling by integrating artificial intelligence in Earth system science, *Nat. Mach. Intell.*, 3, 667–674, <https://doi.org/10.1038/s42256-021-00374-3>, 2021.

- 715 Jeppesen, J. H., Jacobsen, R. H., Inceoglu, F., and Toftegaard, T. S.: A cloud detection algorithm for satellite imagery based on deep learning, *Remote Sens. Environ.*, 229, 247–259, <https://doi.org/10.1016/j.rse.2019.03.039>, 2019.
- Jiao, L., Huo, L., Hu, C., and Tang, P.: Refined UNet: UNet-Based Refinement Network for Cloud and Shadow Precise Segmentation, *Remote Sens.*, 12, <https://doi.org/10.3390/rs12122001>, 2020.
- Jones, N.: How machine learning could help to improve climate forecasts, *Nature*, 548, 379–379, <https://doi.org/10.1038/548379a>, 2017.
- 720 Jordahl, K., Bossche, J. V. D., Fleischmann, M., Wasserman, J., McBride, J., Gerard, J., Tratner, J., Perry, M., Badaracco, A. G., Farmer, C., Hjelle, G. A., Snow, A. D., Cochran, M., Gillies, S., Culbertson, L., Bartos, M., Eubank, N., Maxalbert, Bilogur, A., Rey, S., Ren, C., Arribas-Bel, D., Wasser, L., Wolf, L. J., Journois, M., Wilson, J., Greenhall, A., Holdgraf, C., Filipe, and Leblanc, F.: *geopandas/geopandas: v0.8.1*, <https://doi.org/10.5281/ZENODO.3946761>, 2020.
- Karpatne, A., Ebert-Uphoff, I., Ravela, S., Babaie, H. A., and Kumar, V.: Machine Learning for the Geosciences: Challenges and Opportunities, *IEEE Trans. Knowl. Data Eng.*, 31, 1544–1554, <https://doi.org/10.1109/TKDE.2018.2861006>, 2019.
- 725 Kingma, D. P. and Ba, J.: Adam: A Method for Stochastic Optimization, <https://doi.org/10.48550/ARXIV.1412.6980>, 2014.
- Kühnlein, M., Appelhans, T., Thies, B., and Nauss, T.: Improving the accuracy of rainfall rates from optical satellite sensors with machine learning — A random forests-based approach applied to MSG SEVIRI, *Remote Sens. Environ.*, 141, 129–143, <https://doi.org/https://doi.org/10.1016/j.rse.2013.10.026>, 2014.
- 730 Le Goff, M., Tourneret, J.-Y., Wendt, H., Ortner, M., and Spigai, M.: Deep learning for cloud detection, in: 8th International Conference of Pattern Recognition Systems (ICPRS 2017), pp. 1–6, <https://doi.org/10.1049/cp.2017.0139>, 2017.
- LeCun, Y., Bengio, Y., and Hinton, G.: Deep learning, *Nature*, 521, 436–444, <https://doi.org/10.1038/nature14539>, 2015.
- Lee, Y., Kummerow, C. D., and Ebert-Uphoff, I.: Applying machine learning methods to detect convection using Geostationary Operational Environmental Satellite-16 (GOES-16) advanced baseline imager (ABI) data, *Atmos. Meas. Tech.*, 14, 2699–2716, <https://doi.org/10.5194/amt-14-2699-2021>, 2021.
- 735 Leinonen, J., Guillaume, A., and Yuan, T.: Reconstruction of Cloud Vertical Structure With a Generative Adversarial Network, *Geophys. Res. Lett.*, 46, 7035–7044, <https://doi.org/10.1029/2019GL082532>, 2019.
- Li, R., Liu, W., Yang, L., Sun, S., Hu, W., Zhang, F., and Li, W.: DeepUNet: A Deep Fully Convolutional Network for Pixel-Level Sea-Land Segmentation, *IEEE J. Sel. Top. Appl. Earth Obs. Remote Sens.*, 11, 3954–3962, <https://doi.org/10.1109/JSTARS.2018.2833382>, 2018.
- 740 Liu, Y., Racah, E., Prabhat, M., Correa, J., Khosrowshahi, A., Lavers, D., Kunkel, K., Wehner, M., and Collins, W.: Application of Deep Convolutional Neural Networks for Detecting Extreme Weather in Climate Datasets, <https://doi.org/arXiv:1605.01156>, 2016.
- Marais, W. J., Holz, R. E., Reid, J. S., and Willett, R. M.: Leveraging spatial textures, through machine learning, to identify aerosols and distinct cloud types from multispectral observations, *Atmos. Meas. Tech.*, 13, 5459–5480, <https://doi.org/10.5194/amt-13-5459-2020>, 2020.
- 745 Marchand, R., Mace, G. G., Ackerman, T., and Stephens, G.: Hydrometeor Detection Using Cloudsat—An Earth-Orbiting 94-GHz Cloud Radar, *J. Atmos. Ocean Technol.*, 25, 519–533, <https://doi.org/10.1175/2007JTECHA1006.1>, 2008.
- Mathieu, M., Couprie, C., and LeCun, Y.: Deep multi-scale video prediction beyond mean square error, <https://doi.org/https://doi.org/10.48550/arXiv.1511.05440>, 2016.
- McCandless, T. and Jiménez, P. A.: Examining the Potential of a Random Forest Derived Cloud Mask from GOES-R Satellites to Improve
- 750 Solar Irradiance Forecasting, *Energies*, 13, <https://doi.org/10.3390/en13071671>, 2020.

- Miller, S. D., Forsythe, J. M., Partain, P. T., Haynes, J. M., Bankert, R. L., Sengupta, M., Mitrescu, C., Hawkins, J. D., and Haar, T. H. V.: Estimating Three-Dimensional Cloud Structure via Statistically Blended Satellite Observations, *J. Appl. Meteorol. Climatol.*, 53, 437–455, <https://doi.org/10.1175/JAMC-D-13-070.1>, 2014.
- 755 Noh, Y.-J., Haynes, J. M., Miller, S. D., Seaman, C. J., Heidinger, A. K., Weinrich, J., Kulie, M. S., Niznik, M., and Daub, B. J.: A Framework for Satellite-Based 3D Cloud Data: An Overview of the VIIRS Cloud Base Height Retrieval and User Engagement for Aviation Applications, *Remote Sens.*, 14, 5524, <https://doi.org/10.3390/rs14215524>, 2022.
- Norris, J. R., Allen, R. J., Evan, A. T., Zelinka, M. D., O'Dell, C. W., and Klein, S. A.: Evidence for climate change in the satellite cloud record, *Nature*, 536, 72–75, <https://doi.org/10.1038/nature18273>, 2016.
- 760 Pan, X., Lu, Y., Zhao, K., Huang, H., Wang, M., and Chen, H.: Improving Nowcasting of Convective Development by Incorporating Polarimetric Radar Variables Into a Deep-Learning Model, *Geophys. Res. Lett.*, 48, e2021GL095302, <https://doi.org/https://doi.org/10.1029/2021GL095302>, 2021.
- Platnick, S., Meyer, K. G., King, M. D., Wind, G., Amarasinghe, N., Marchant, B., Arnold, G. T., Zhang, Z., Hubanks, P. A., Holz, R. E., Yang, P., Ridgway, W. L., and Riedi, J.: The MODIS Cloud Optical and Microphysical Products: Collection 6 Updates and Examples From Terra and Aqua, *IEEE Trans. Geosci. Remote Sens.*, 55, 502–525, <https://doi.org/10.1109/TGRS.2016.2610522>, 2017.
- 765 Rasp, S., Pritchard, M. S., and Gentine, P.: Deep learning to represent sub-grid processes in climate models, *PNAS*, 115, 9684–9689, <https://doi.org/10.1073/pnas.1810286115>, 2018.
- Reichstein, M., Camps-Valls, G., Stevens, B., Jung, M., Denzler, J., Carvalhais, N., and Prabhat: Deep learning and process understanding for data-driven Earth system science, *Nature*, 566, 195–204, <https://doi.org/10.1038/s41586-019-0912-1>, 2019.
- 770 Rolnick, D., Donti, P. L., Kaack, L. H., Kochanski, K., Lacoste, A., Sankaran, K., Ross, A. S., Milojevic-Dupont, N., Jaques, N., Waldman-Brown, A., Luccioni, A. S., Maharaj, T., Sherwin, E. D., Mukkavilli, S. K., Kording, K. P., Gomes, C. P., Ng, A. Y., Hassabis, D., Platt, J. C., Creutzig, F., Chayes, J., and Bengio, Y.: Tackling Climate Change with Machine Learning, *ACM Comput. Surv.*, 55, 1–96, <https://doi.org/10.1145/3485128>, 2022.
- Ronneberger, O., Fischer, P., and Brox, T.: U-Net: Convolutional Networks for Biomedical Image Segmentation., in: *Medical Image Computing and Computer-Assisted Intervention – MICCAI 2015*, edited by Navab, N., Hornegger, J., Wells, W. M., and Frangi, A. F., pp. 234–241, Springer International Publishing, Cham, [https://doi.org/https://doi.org/10.1007/978-3-319-24574-4\\_28](https://doi.org/https://doi.org/10.1007/978-3-319-24574-4_28), 2015.
- 775 Runge, J., Bathiany, S., Bollt, E., Camps-Valls, G., Coumou, D., Deyle, E., Glymour, C., Kretschmer, M., Mahecha, M. D., Muñoz-Marí, J., van Nes, E. H., Peters, J., Quax, R., Reichstein, M., Scheffer, M., Schölkopf, B., Spirtes, P., Sugihara, G., Sun, J., Zhang, K., and Zscheischler, J.: Inferring causation from time series in Earth system sciences, *Nat. Commun.*, 10, 2553, <https://doi.org/10.1038/s41467-019-10105-3>, 2019.
- 780 Schmetz, J., Pili, P., Tjemkes, S., Just, D., Kerkmann, J., Rota, S., and Ratier, A.: An Introduction to Meteosat Second Generation (MSG), *BAMS*, 83, 977–992, [https://doi.org/10.1175/1520-0477\(2002\)083<0977:AITMSG>2.3.CO;2](https://doi.org/10.1175/1520-0477(2002)083<0977:AITMSG>2.3.CO;2), 2002.
- Seiz, G. and Davies, R.: Reconstruction of cloud geometry from multi-view satellite images, *Remote Sens. Environ.*, 100, 143–149, <https://doi.org/10.1016/j.rse.2005.09.016>, 2006.
- Shepherd, T. G.: Atmospheric circulation as a source of uncertainty in climate change projections, *Nat. Geosci.*, 7, 703–708, <https://doi.org/10.1038/ngeo2253>, 2014.
- 785 Sieglaff, J., Hartung, D., Feltz, W., Cronce, L., and Lakshmanan, V.: A Satellite-Based Convective Cloud Object Tracking and Multipurpose Data Fusion Tool with Application to Developing Convection, *J. Atmos. Ocean. Technol.*, 30, 510–525, <https://doi.org/10.1175/JTECH-D-12-00114.1>, 2013.

- Steiner, M., Houze, R. A., and Yuter, S. E.: Climatological Characterization of Three-Dimensional Storm Structure from  
790 Operational Radar and Rain Gauge Data, *J. Climatol. Appl. Meteorol.*, 34, 1978–2007, [https://doi.org/10.1175/1520-0450\(1995\)034<1978:CCOTDS>2.0.CO;2](https://doi.org/10.1175/1520-0450(1995)034<1978:CCOTDS>2.0.CO;2), 1995.
- Stephens, G. L., Vane, D. G., Tanelli, S., Im, E., Durden, S., Rokey, M., Reinke, D., Partain, P., Mace, G. G., Austin, R., L'Ecuyer, T., Haynes, J., Lebsock, M., Suzuki, K., Waliser, D., Wu, D., Kay, J., Gettelman, A., Wang, Z., and Marchand, R.: CloudSat mission: Performance and early science after the first year of operation, *J. Geophys. Res. Atmos.*, 113, <https://doi.org/10.1029/2008JD009982>, 2008.
- 795 Stevens, B. and Bony, S.: What Are Climate Models Missing?, *Science*, 340, 1053–1054, <https://doi.org/10.1126/science.1237554>, 2013.
- Stubenrauch, C. J., Rossow, W. B., Kinne, S., Ackerman, S., Cesana, G., Chepfer, H., Girolamo, L. D., Getzewich, B., Guignard, A., Heidinger, A., Maddux, B. C., Menzel, W. P., Minnis, P., Pearl, C., Platnick, S., Poulsen, C., Riedi, J., Sun-Mack, S., Walther, A., Winker, D., Zeng, S., and Zhao, G.: Assessment of Global Cloud Datasets from Satellites: Project and Database Initiated by the GEWEX Radiation Panel, *BAMS*, 94, 1031–1049, <https://doi.org/10.1175/BAMS-D-12-00117.1>, 2013.
- 800 Tarrío, K., Tang, X., Masek, J. G., Claverie, M., Ju, J., Qiu, S., Zhu, Z., and Woodcock, C. E.: Comparison of cloud detection algorithms for Sentinel-2 imagery, *Science of Remote Sens.*, 2, 100010, <https://doi.org/https://doi.org/10.1016/j.srs.2020.100010>, 2020.
- Thies, B. and Bendix, J.: Satellite based remote sensing of weather and climate: recent achievements and future perspectives, *Meteorol. Appl.*, 18, 262–295, <https://doi.org/10.1002/met.288>, 2011.
- Troyanskaya, O., Cantor, M., Sherlock, G., Brown, P., Hastie, T., Tibshirani, R., Botstein, D., and Altman, R. B.: Missing value estimation  
805 methods for DNA microarrays, *Bioinformatics*, 17, 520–525, <https://doi.org/10.1093/bioinformatics/17.6.520>, 2001.
- van den Heuvel, F., Foresti, L., Gabella, M., Germann, U., and Berne, A.: Learning about the vertical structure of radar reflectivity using hydrometeor classes and neural networks in the Swiss Alps, *Atmos. Meas. Tech.*, 13, 2481–2500, <https://doi.org/10.5194/amt-13-2481-2020>, 2020.
- Vial, J., Dufresne, J.-L., and Bony, S.: On the interpretation of inter-model spread in CMIP5 climate sensitivity estimates, *Clim. Dyn.*, 41,  
810 3339–3362, <https://doi.org/10.1007/s00382-013-1725-9>, 2013.
- Wang, F., Liu, Y., Zhou, Y., Sun, R., Duan, J., Li, Y., Ding, Q., and Wang, H.: Retrieving Vertical Cloud Radar Reflectivity from MODIS Cloud Products with CGAN: An Evaluation for Different Cloud Types and Latitudes, *Remote Sens.*, 15, 816, <https://doi.org/10.3390/rs15030816>, 2023.
- Wang, G., Wang, H., Zhuang, Y., Wu, Q., Chen, S., and Kang, H.: Tropical Overshooting Cloud-Top Height Retrieval from Himawari-8  
815 Imagery Based on Random Forest Model, *Atmosphere*, 12, <https://doi.org/10.3390/atmos12020173>, 2021.
- Wang, S., Chen, W., Xie, S. M., Azzari, G., and Lobell, D. B.: Weakly Supervised Deep Learning for Segmentation of Remote Sensing Imagery, *Remote Sens.*, 12, <https://doi.org/10.3390/rs12020207>, 2020.
- Wang, Z., Zhao, J., Zhang, R., Li, Z., Lin, Q., and Wang, X.: UATNet: U-Shape Attention-Based Transformer Net for Meteorological Satellite Cloud Recognition, *Remote Sens.*, 14, <https://doi.org/10.3390/rs14010104>, 2022.
- 820 Watson-Parris, D.: Machine learning for weather and climate are worlds apart, *Philos. Trans. Royal Soc. A*, 379, 20200098, <https://doi.org/10.1098/rsta.2020.0098>, 2021.
- Wieland, M., Li, Y., and Martinis, S.: Multi-sensor cloud and cloud shadow segmentation with a convolutional neural network, *Remote Sens. Environ.*, 230, <https://doi.org/10.1016/j.rse.2019.05.022>, 2019.
- Zantedeschi, V., Falasca, F., Douglas, A., Strange, R., Kusner, M. J., and Watson-Parris, D.: Cumulo: A Dataset for Learning Cloud Classes,  
825 <https://doi.org/https://doi.org/10.48550/arXiv.1911.04227>, 2022.

Zhang, D., He, Y., Li, X., Zhang, L., and Xu, N.: PrecipGradeNet: A New Paradigm and Model for Precipitation Retrieval with Grading of Precipitation Intensity, *Remote Sens.*, 15, <https://doi.org/10.3390/rs15010227>, 2023.

Zhang, Z., Ackerman, A. S., Feingold, G., Platnick, S., Pincus, R., and Xue, H.: Effects of cloud horizontal inhomogeneity and drizzle on remote sensing of cloud droplet effective radius: Case studies based on large-eddy simulations, *J. Geophys. Res. Atmos.*, 117, <https://doi.org/https://doi.org/10.1029/2012JD017655>, 2012.

830